Copyright © 2000, by the author(s).
All rights reserved.

Permission to make digital or hard copies of all or part of this work for personal or classroom use is granted without fee provided that copies are not made or distributed for profit or commercial advantage and that copies bear this notice and the full citation on the first page. To copy otherwise, to republish, to post on servers or to redistribute to lists, requires prior specific permission.

DEEP SUBMICRON PHOTORESIST MODELING AND PARAMETER EXTRACTION

by

Junwei Bao

Memorandum No. UCB/ERL M00/28

15 May 2000

DEEP SUBMICRON PHOTORESIST MODELING AND PARAMETER EXTRACTION

by

Junwei Bao

Memorandum No. UCB/ERL M00/28

15 May 2000

ELECTRONICS RESEARCH LABORATORY

College of Engineering
University of California, Berkeley
94720

Deep Submicron Photoresist Modeling and Parameter Extraction

by Junwei Bao

Research Project

Submitted to the Department of Electrical Engineering and Computer Science, University of California at Berkeley, in partial satisfaction of the requirements for the degree of **Master of Science, Plan II.**

Approval for the Report and Comprehensive Examination:

Committee:

Professor Costas J. Spanos

Research Advisor

5/15/2000

(Date)

* * * * * * *

Professor Andrew R. Neureuther

Second Reader

May 15 2000

(Date)

Abstract

Lithography is the key technology driver for the semiconductor industry. The improvement of the lithographic resolution provides much of the momentum for the continued growth of the industry. As DUV lithography becomes mainstream, efficient process development is becoming crucial, due to the high costs associated with the equipment and materials, and continually shortened time-to-market.

Chemically amplified resist is the workhorse for pattern transfer in the DUV lithography generation. Much work has been done in studying the physical and chemical mechanisms in the lithography process. However, all of the existing models have been shown to be inadequate to capture some phenomena observed in DUV lithography, such as deprotection induced thickness loss and dynamic quenching reaction effect. In this report, we propose new static models that incorporate the quencher effect, and a physically based dynamic model for the post exposure bake step.

Parameter extraction and simulator calibration are essential simulation steps. Only after we have accurately calibrated the simulator can we fully utilize all the fab data and effectively combine the modeling, analysis and optimization tools to dramatically cut the development and production costs. A parameter extraction framework using adaptive simulated annealing as the optimization engine is proposed, and experimental data on two DUV resists are used to extract their corresponding model parameters.

Table of Contents

Table of Contents i
Chapter 1 Introduction 1
1.1 BACKGROUNDS AND MOTIVATION 1
1.2 THESIS ORGANIZATION 2
Chapter 2 Modeling Chemically Amplified Photoresist Behavior for DUV Lithography 3
2.1 INTRODUCTION 3
2.2 BASIC MECHANISM FOR CHEMICALLY AMPLIFIED POSITIVE DUV PHOTORESIST 4
2.3 CONVENTIONAL MODELS FOR EXPOSURE, BAKE AND DEVELOPMENT 5
2.3.1 Exposure Model *5*
2.3.2 PEB Model *6*
2.3.3 Development model *7*
2.4 STATIC MODELS FOR DEPROTECTION CONSIDERING THE QUENCHING EFFECT 7
2.4.1 Reduced Effective Dose Model *7*
2.4.2 Quencher Reaction Model *8*
2.5 DYNAMIC MODEL FOR DEPROTECTION INDUCED THICKNESS LOSS 9
2.5.1 PEB Mechanism and Physical Model *9*
2.5.2 Initial and Boundary Conditions *13*
2.6 SUMMARY 14
Chapter 3 Numerical Implementation of DITL Model with Moving-Boundary Finite Difference Method15
3.1 INTRODUCTION 15
3.2 FINITE DIFFERENCE FORMULATION 15
3.3 MOVING BOUNDARY SETUP 19
3.4 SUMMARY 21
Chapter 4 Adaptive Simulated Annealing and Multilayer Thin Film Thickness Extraction 23
4.1 INTRODUCTION 23
4.2 ADAPTIVE SIMULATED ANNEALING 23
4.2.1 Global Minimization Problem *23*
4.2.2 Simulated Annealing *24*
4.2.3 Adaptive Simulated Annealing *26*
4.3 MULTILAYER THIN FILM THICKNESS EXTRACTION 27
4.3.1 Multilayer Thin Film Reflection Formulation *27*
4.3.2 Multilayer Thin Film Thickness Extraction Using ASA *31*
4.4 SUMMARY 32
Chapter 5 Experimental Setup and Parameter Extraction Results 33
5.1 INTRODUCTION 33
5.2 PARAMETER EXTRACTION FRAMEWORK 33
5.3 EXPERIMENT SETUP 34
5.3.1 Experiment Design *34*
5.3.2 Resist Thickness Extraction *35*
5.4 PARAMETER EXTRACTION WITH STATIC PROCESS MODELS 39
5.4.1 Validation of Static Models for Deprotection Considering the Quenching Effect *39*
5.4.2 Parameter Extraction with Static Process Models *40*
5.5 PARAMETER EXTRACTION WITH DYNAMIC DITL MODEL 44
5.5.1 Dynamic DITL Model Validation *44*
5.5.2 Parameter Extraction using Dynamic DITL Model *46*
5.6 SUMMARY 49
Chapter 6 Conclusion 51

6.1 SUMMARY 51
6.2 FUTURE WORK 51
References 55
Appendix A List of Figures 59
Appendix B List of Symbols 61

Acknowledgements

I would like to thank my advisor, Professor Costas Spanos, for his valuable guidance, support and encouragement during the last three years. Especially I am very grateful to him for the time he spent on this thesis. Many thanks to Professor Andy Neureuther for his invaluable comments and suggestions he gave when proofreading this report.

Special thanks to Xinhui Niu and Nickhil Jakatdar for their help, mentoring and friendship during this work. I would like to thank the friendship and support from the other BCAMers: Jason Cain, Runzi Chang, Mareike Claassen, Roawen Chen, Scott Eitepence, Darin Fisher, Ralph Foong, Mason Freed, Andy Gleckman, Steve Hu, Anna Ison, Michiel Kruger, Jae-wook Lee, John Lin, John Masacchio, Matt Onsum, Professor Kameshwar Poolla, Johan Saleh, Nickhil Vaidya, Jiangxin Wang, Haolin Zhang, Dongwu Zhao. I am also grateful to the staff at BCAM and Microlab: Tim Duncan, Diane Chang, Debra Krauss, Katalin Voros, Bob Hamilton, Kim Chan, Charlie Williams, Cheryl Craigwell. Many thanks to my friends in Cory Hall: Yashesh Shroff, Fan Piao, Mosong Cheng, Ebo Croffie, Tom Pistor, Kostas Adam, Bo Wu, Yunfei Deng.

Thanks to our friends in the semiconductor inductry: Joe Bendik, Ramkumar Subramanian, Bharath Rangarajan, Chris Mack, Matt Hankinson, Piotr Zalicki, Bob Socha, Rick Dill, for their support and mentorship.

This work was supported by the UC-SMART program under contract #SM97-01, and by the following participating companies: Advanced Micro Devices, Atmel Corp., Applied Materials, Asyst Technologies, BOC Edwards, Cymer, Etec Systems, Intel Corp., KLA-TENCOR, Lam Research Corp., Nanometrics, Nikon Research Corp., Novellus Systems, Silicon Valley Group, and Texas Instruments.

Chapter 1 Introduction

1.1 Backgrounds and Motivation

Lithography is the key technology driver for the semiconductor industry [1]. The improvement of lithographic resolution provides much of the momentum for the continued growth of the industry. Lithography is also a significant economic factor, currently representing over thirty-five percent of the chip manufacturing cost. This necessitates the use of simulation to reduce the number of characterization experiments devoted to developing new recipes, hence saving expensive equipment time and reducing time-to-market.

There are three important elements required in order to simulate a process [1]: models, simulators, and calibration/validation. Models provide a mental image of reality, formalized in mathematical formulae, simulators implement models with computer codes, and finally the simulated results need to be compared to relevant experimental data to determine numeric parameter values and to demonstrate suitability for purpose. A good physical model can be used to provide helpful insight to a process still in research or in the early stage of development. During later stages, a well-calibrated simulator can be used for optimization, sensitivity analysis, and process diagnosis.

There are many academic (SAMPLE, SPLAT, TEMPEST, STORM, [2]) and commercial (PROLITH [3], SOLID-C [4], etc.) *Technology Computer-Aided Design* (TCAD) tools that simulate the entire lithography process and use efficient numerical models. However, as more new resist types and processes are developed for lithography, improvements are needed in resist modeling of during exposure, bake, and develop [5]. In this thesis, we propose new static models that incorporate the quencher effect, and a physically based dynamic model for the *Post Exposure Bake* (PEB) step.

Parameter extraction and simulator calibration are essential simulation steps. Only after we have accurately calibrated the simulator can we fully utilize all the fab data and effectively combine the modeling, analysis and optimization tools to dramatically cut the development and

production costs. *Adaptive Simulated Annealing* (ASA) is extensively used in this work in order to calibrate the models we propose.

1.2 Thesis Organization

This thesis begins with an overview of chemically amplified DUV resist chemistry and the respective models. We then propose two new models that include the quenching effect, the reduced effective dose, and the quencher reaction. We also derive the dynamic model for *Deprotection Induced Thickness Loss* (DITL) from the physical mechanism of resist bake. In chapter 3, the dynamic DITL model is discretized using the finite difference method, and a moving boundary method is used to solve the numerical problem. Chapter 4 discusses the ASA optimization engine for parameter extraction, as well as the practical problems of thin film thickness extraction encountered in the experiment. Chapter 5 begins with a formal description of the parameter extraction framework, and addresses some practical issues about the experimental setup. Chapter 5 also describes how static model resist parameters are extracted and introduced into the dynamic model parameter extraction framework to help reduce the problem dimension. Chapter 5 ends with dynamic model validation and parameter extraction. Finally, conclusions of this work are presented in chapter 6.

Chapter 2 Modeling Chemically Amplified Photoresist Behavior for DUV Lithography

2.1 Introduction

Chemically Amplified Resist (CAR) is the workhorse for pattern transfer in the DUV lithography generation. Ito and Wilson first proposed the use of an aryl onium salt [15], and triphenylsulfonium salts have been studied extensively as PAGs. In CARs, a strong acid is formed during the exposure process, and it works as a catalyst for a chemical reaction that deblocks the polymer resin (for positive resist) during PEB. This makes the exposure kinetics quite different from that of the I-line resists used in the past.

Much work has been done in describing the physical and chemical processes that occur during PEB, especially in studying the acid transport mechanism. The diffusivity behavior has been described as constant [16], linear and exponential concentration dependent [6] [18] [17]. Zuniga and Neureuther found that simple Fickean model does not adequately describe line width growth versus PEB time and they were able to fit the line width growth versus PEB time data with a case II type reaction driven diffusion model assuming the exponential dependent on the deprotection site concentration. But all of these models have been shown to be inadequate to capture some phenomena recently observed in DUV lithography, such as *Deprotection Induced Thickness Loss* (DITL) and dynamic quenching reaction effect. Recently models that include these effects have been proposed and compared with experimental data [11] [10] [12]. They have offered useful insight to understanding the PEB reaction mechanisms and to explaining some recent experimental results [10] [13].

In this chapter we begin with a discussion of the basic resist chemistry and the overall mechanism for positive chemically amplified photoresist. Next, we discuss the reaction mechanism of the quencher with the acid and include it in a modified static model. Finally, we propose a physically based dynamic model to predict DITL during the PEB step.

2.2 Basic Mechanism for Chemically Amplified Positive DUV Photoresist

Chemically amplified positive photoresists are typically composed of a *Photo Acid Generator* (PAG), a polymer resin soluble in an aqueous base developer, a protecting t-BOC group which reacts with the resin and forms side chains to slow down its solubility, and possibly some dyes and additives along with the casting solvent.

During the exposure process the photon energy makes the PAG decompose and generate acid ions. A common PAG reaction is shown below [17] [18]:

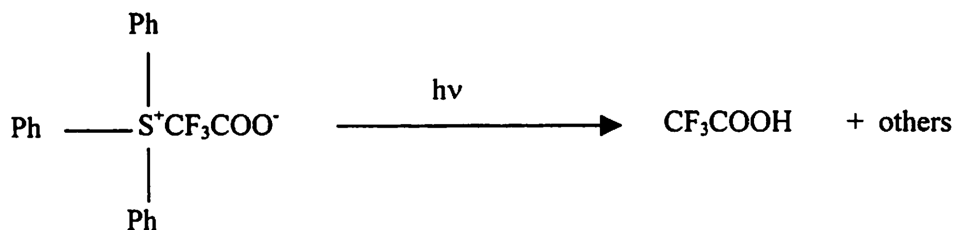

Figure 2.1. PAG decomposition during exposure (Ph represents benzyl.)

The generated acid ions attack the side chains (t-BOC) of the polymer (deprotection) and generate more acid during the PEB step, as shown in Figure 2.2. Thus the acid concentration is amplified during PEB, and the resin without side chains can then be dissolved in the aqueous base developer. There is another byproduct, $CH_2C(CH_3)_2$, created during this reaction. It is volatile and will evaporate, causing film shrinkage in exposed areas. The amount of shrinkage depends on the molecular weight of the blocking groups.

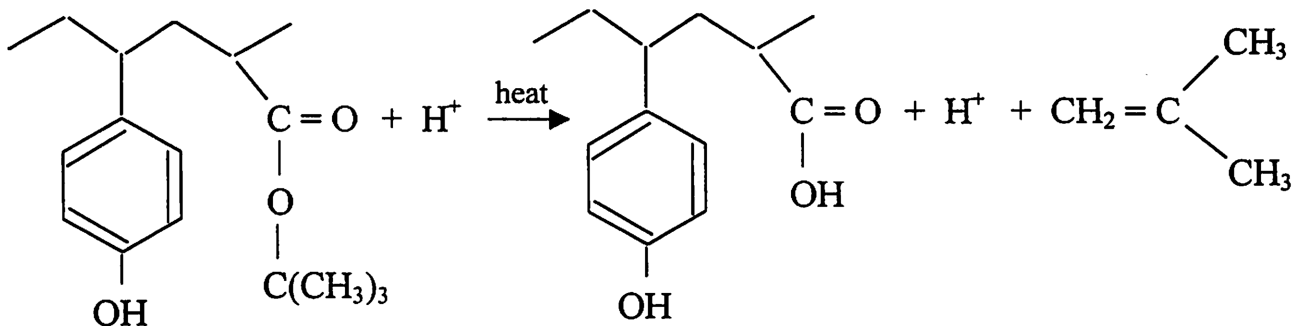

Figure 2.2. Deprotection during PEB.

After the PEB step, the developer is applied to resolve the deprotected resist, and transfer the pattern on the mask to the resist on the wafer.

2.3 Conventional Models for Exposure, Bake and Development

2.3.1 Exposure Model

The exposure process in chemically amplified resists has been modeled by Byes et al [18]. The applied dose is first converted into an effective dose, which is coupled into the resist as a function of depth. This depth dependence of the exposure dose uses a simplified form of the full wave equation, as shown in Eq. 2.1,

$$\text{Dose}(z) = D_s\left(e^{-\alpha(d-z)} + |\tilde{r}|^2 e^{-\alpha(d+z)} - 2|\tilde{r}|e^{-\alpha d}\cos\left(\frac{4\pi nz}{\lambda} + \varphi_0\right)\right), \qquad (2.1)$$

where D_s is the applied dose in mJ/cm^2, corrected by the reflectivity at the air-resist interface, α is the absorption coefficient of the resist film in nm^{-1}, d is the film thickness in nm, n is the real part of the refractive index, λ is the exposure wavelength in nm, $\tilde{r}$ is the complex reflectivity coefficient of the resist/underlayer interface, φ_0 is the phase shift due to the complex reflectivity coefficient $\tilde{r}$, and z is the distance from the resist/underlayer interface in the resist in nm. This dose is averaged from 0 to d to get the effective dose coupled into the resist.

$$\text{Dose} = \frac{1}{d}\int_0^d \text{Dose}(z)\,dz \qquad (2.2)$$

This effective dose is converted into the acid concentration just after the exposure process as follows,

$$[\text{Acid}] = [\text{PAG}]_0(1 - e^{-C\cdot\text{Dose}}) \qquad (2.3)$$

where [Acid] is the acid concentration right after exposure, $[PAG]_0$ is the initial PAG concentration, C is the photoacid formation coefficient, and Dose is the average dose given by

(2.2). Both [Acid] and $[PAG]_0$ are in units of nm^{-3}. We normalize the acid concentration to $[PAG]_0$ and express it as $u = [Acid]/[PAG]_0$ in later sections of this work.

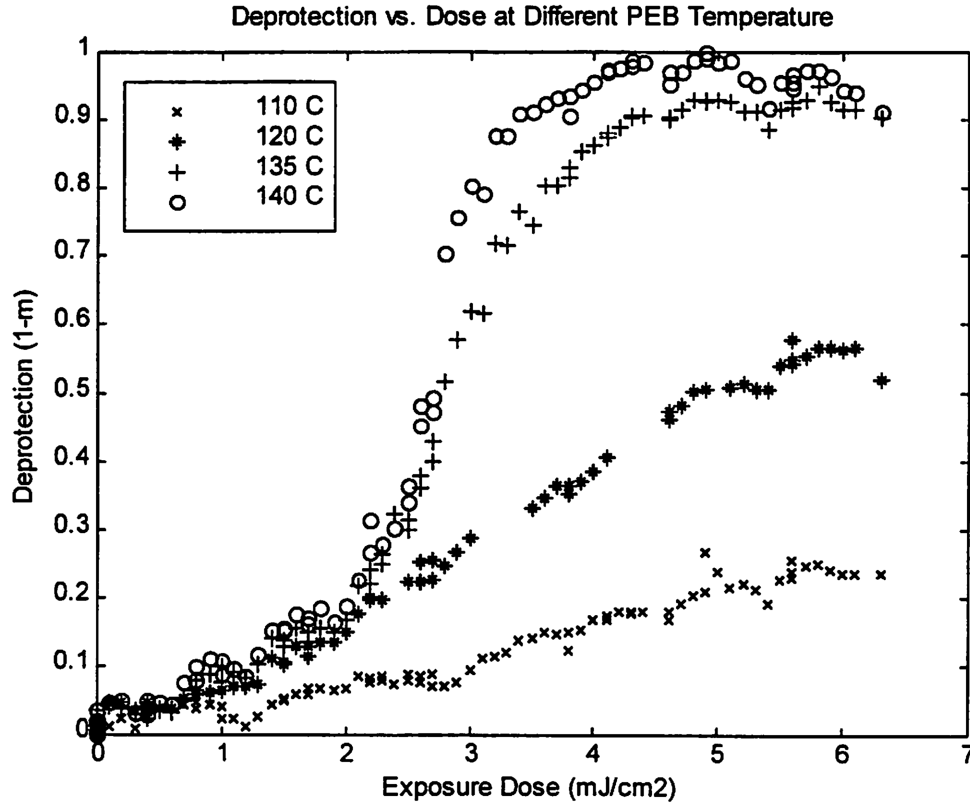

Figure 2.3. Deprotection vs. dose at various PEB temperatures.

2.3.2 PEB Model

During the PEB process, the t-BOC blocked polymer undergoes acidolysis to generate the soluble hydroxyl group in the presence of acid and heat [7]. In the conventional PEB model, the deprotection is calculated as follows,

$$m = \mathrm{Exp}\left[-k_{amp}\left(\frac{1-e^{-k_{loss}t}}{k_{loss}}\right)\cdot u\right] \tag{2.4}$$

where m is the normalized concentration of unreacted blocking sites, k_{amp} is the acid amplification factor, and k_{loss} is the acid loss factor. Both k_{amp} and k_{loss} are in units of sec^{-1}, and follow an Arrhenius behavior:

$$k_{amp} = A_{amp} \times \mathrm{Exp}\left(-\frac{E_{amp}}{RT}\right) \tag{2.5}$$

$$k_{loss} = A_{loss} \times \mathrm{Exp}\left(-\frac{E_{loss}}{RT}\right), \tag{2.6}$$

where R (=1.99 $cal \cdot mol^{-1} \cdot K^{-1}$) is the universal gas constant, and T is the temperature in Kelvin.

The models introduced above, however, do not account for the initial delay in the ramping up of the deprotection vs. dose curve (Figure 2.3) at different temperatures. We attribute this to the effect of the quencher designed into the resist or absorbed from the environment. In section 2.4, we propose two models to account for this effect.

2.3.3 Development model

We can use the standard Mack model [19] to model the development process.

$$R(m) = R_{max} \frac{(a+1)(1-m)^{n_s}}{a+(1-m)^{n_s}} + R_{min} \tag{2.7}$$

$$a = \frac{n_s + 1}{n_s - 1}(1 - m_{th})^{n_s} \tag{2.8}$$

where R_{max} and R_{min} are the maximum and the minimum development rates, respectively, in nm/sec, m_{th} is the value of m at the inflection point of the function, called the threshold PAC concentration, and n_s is the dissolution selectivity parameter, which is determined by the resist dissolution reaction.

2.4 Static Models for Deprotection Considering the Quenching effect

2.4.1 Reduced Effective Dose Model

From Figure 2.3, we can see that the amount of deprotection starts ramping up after a certain dose. This motivates us to model the effect of the quencher as a fixed amount of effective quenching dose, and the effective dose that generates the acid in Eq. 2.3 as the difference of the

dose coupled into the resist and this effective quenching dose. So the acid generation model (2.3) is changed as follows:

$$[\text{Acid}] = [\text{PAG}]_0\left(1 - e^{-C\cdot \text{Dose}_{\text{eff}}}\right) = [\text{PAG}]_0\left(1 - e^{-C\cdot(\text{Dose} - \text{Dose}_q)}\right) \quad (2.9)$$

The relative quencher concentration can then be calculated as:

$$Q = 1 - e^{-C\cdot \text{Dose}_q}, \quad (2.10)$$

where Dose_{eff} is the effective dose corrected by the quenching effect, and Dose_q is the effective quenching dose.

This model describes quenching as a two-step process: the initial quenching reaction step, in which all the acid generated by exposure is immediately neutralized by the basic quencher, and the actual acid generation step, in which the acid generated will be amplified and deprotect the resin during PEB. The resulting equations are easy to solve, and can fit the deprotection curve very well for the second step, as can be seen in Chapter 5. However, they cannot explain the initial slow ramping in Figure 2.3. The model introduced in the next section accommodates this initial step.

2.4.2 Quencher Reaction Model

In reality, the quenching continues all through the PEB process, and the acid is neutralized by the quencher, as shown below:

$$\text{Acid} + Q \leftrightarrow H_2O$$

The acid and the quencher concentrations during this process are described by the following differential equation,

$$\frac{\partial}{\partial t}[\text{Acid}]_t = -k_\alpha [\text{Acid}]_t [Q]_t \quad (2.11)$$

where k_α is the neutralization reaction coefficient modeled by an Arrhenius temperature relation,

$$k_\alpha = A_\alpha \times \text{Exp}\left(-\frac{E_\alpha}{RT}\right), \quad (2.12)$$

$[Acid]_t$ and $[Q]_t$ are the acid and quencher concentrations, respectively, in nm^{-3} at time t. During this process, the difference between the acid and quencher concentrations remains constant:

$$[Acid]_t - [Q]_t = [Acid]_0 - [Q]_0, \qquad (2.13)$$

where $[Acid]_0$ and $[Q]_0$ are the initial acid and quencher concentrations before PEB. Solving equations (2.11) and (2.13), we get the acid concentration as a function of the PEB time:

$$[Acid]_t = \frac{[Acid]_0 - [Q]_0}{1 - \frac{[Q]_0}{[Acid]_0} Exp(-k_\alpha([Acid]_0 - [Q]_0)t)} \qquad (2.14)$$

During PEB, the amount of deprotection is modeled by the following expression,

$$\frac{\partial}{\partial t}[M]_t = -k_{amp}[Acid]_t[M]_t \qquad (2.15)$$

where $[M]_t$ is the concentration of protected sites at time t, and k_{amp} is modeled by Eq. (2.5). Substituting Eq. (2.14) into Eq. (2.15), and solving for $[M]_t$, we obtain the normalized protected site concentration m:

$$m \equiv \frac{[M]_t}{[M]_0} = \left[\frac{[Acid]_0 Exp(k_\alpha([Acid]_0 - [Q]_0)t) - [Q]_0}{[Acid]_0 - [Q]_0}\right]^{-\frac{k_{amp}}{k_\alpha}} \qquad (2.16)$$

This equation differs from previously reported models, such as Eq. (2.4), in that it models the quenching process all through the PEB step, accommodating both the initial deprotection delay and the later ramping up in Figure 2.3, as can be seen in Chapter 5.

2.5 Dynamic model for Deprotection Induced Thickness Loss

2.5.1 PEB Mechanism and Physical Model

One of the assumptions in previous PEB models is that the resist volume remains constant, and that the acid concentration changes only due to chemical reactions and diffusion. However, it is well known that there is a certain amount of volume shrinkage (e.g., about 5% for Shipley's UV5) for chemically amplified resist. This volume shrinkage changes the acid

concentration, and affects the acid diffusion and deprotection. We propose the following physical model to describe the chemical reaction and diffusion dynamics.

During the exposure step, the photo-acid generators produce acid upon interaction with photons. The initial acid concentration can be calculated from the light intensity distribution within the resist. During the PEB step, the resist is baked to high temperature, resulting in deprotection reaction and chemical diffusion. Figure 2.4 illustrates the initial, deprotection and diffusion steps in three consecutive volume elements (acid loss mechanism is not illustrated).

With sufficient energy, the acid molecules attack the polymer side-chains at a certain reaction rate (k_2), which follows an Arrhenius behavior with temperature, generating a volatile group, and causing deprotection. There is also an acid loss mechanism due to neutralization with parasitic base at a rate of k_{loss} (here we use a simplified assumption that the base concentration is constant). This process is illustrated in figure 2.2 and in the middle of figure 2.4, and can be modeled by the following expressions:

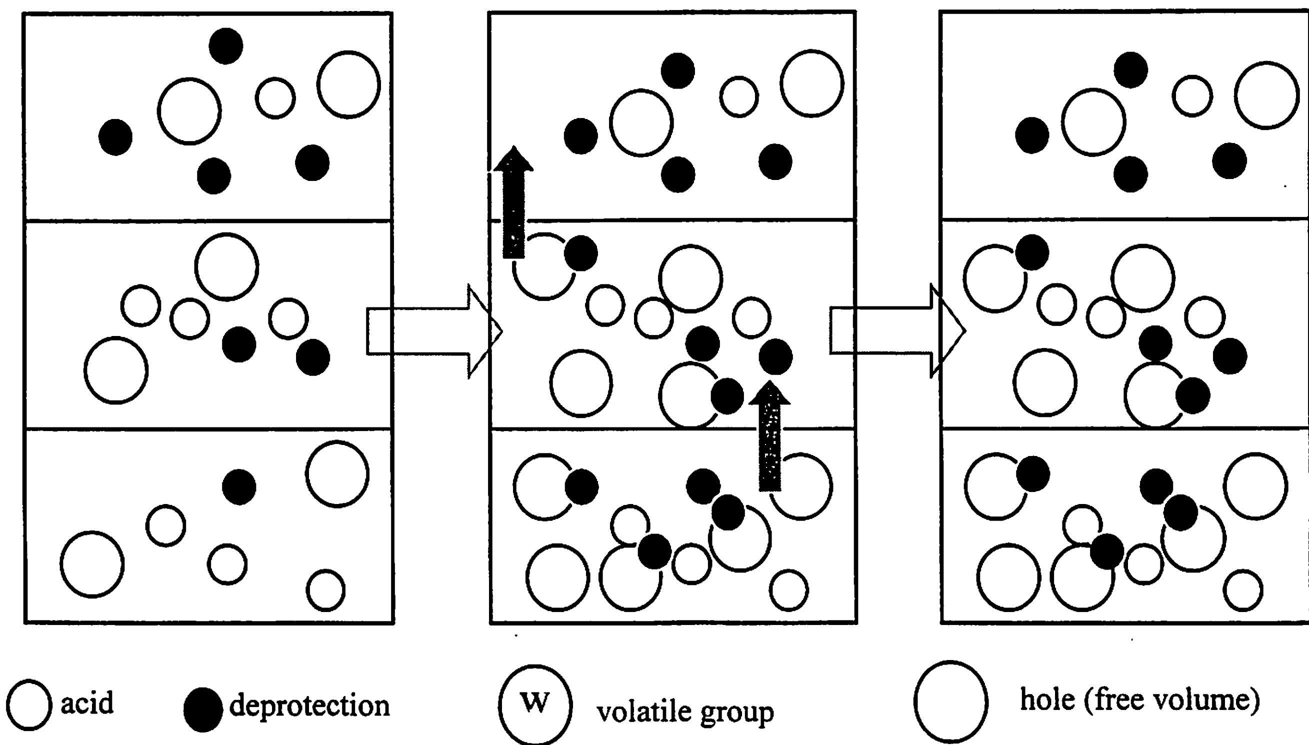

Figure 2.4. Deprotection and diffusion during PEB.

$$\frac{\partial}{\partial t} v = k_2 u(1 - v) \tag{2.17}$$

$$\frac{\partial}{\partial t}(u\omega) = -k_{loss} u\omega \tag{2.18}$$

$$\frac{\partial}{\partial t}(w\omega) = k_1 k_2 u(1 - v)\omega \tag{2.19}$$

In the above three equations, $\omega = \omega(z,t)$ is the size of volume element, v is the portion of deprotection ranging from 0 to 1, u and w are acid and volatile group concentrations normalized to the initial PAG concentration $[PAG]_0$, respectively, k_1 is a constant used to convert the percentage deprotection to volatile group concentration. Because the size of the volume element is not constant during this process, we cannot take ω out of the time derivative and cancel it with the ω on the right-hand side.

Meanwhile, the acid and the volatile group molecules diffuse through the resist with diffusivity D_u and D_w, respectively. The acid diffusivity D_u is typically modeled as an exponential function of free volume [9] with a pre-exponent term D_{u0}. When a volatile molecule diffuses, it leaves a void, or free volume, behind, and fills up another void in its new position, as illustrated in the right figure in figure 2.4 and modeled by the following equations:

$$\frac{\partial}{\partial t}(u\omega) = \nabla \bullet (D_u \nabla u)\omega \tag{2.20}$$

$$D_u = D_{u0} \mathrm{Exp}(ah) \tag{2.21}$$

$$\frac{\partial}{\partial t}(w\omega) = \nabla \bullet (D_w \nabla w)\omega \tag{2.22}$$

$$\frac{\partial}{\partial t}(h\omega) = -\nabla \bullet (D_w \nabla w)\omega \tag{2.23}$$

where h is the free volume concentration normalized to the initial PAG concentration $[PAG]_0$, and the derivatives in the gradients and divergences on the right-hand side of the equations above

are with respect to the coordinate system fixed on the resist. As the resist shrinks during PEB, this coordinate system moves relative to the lab coordinate system.

Once generated, the free volume also collapses with a rate of k_3. It is this polymer relaxation process that causes the resist volume shrinkage during PEB, as described by the following equations:

$$\frac{\partial}{\partial t}(h\omega) = (-k_3 h\omega) \tag{2.24}$$

$$\frac{\partial}{\partial t}\omega = -k_4 k_3 h\omega \tag{2.25}$$

where k_4 is a constant used to convert the number of collapsed voids to volume shrinkage.

In reality, all of the three mechanisms exist simultaneously, so by combining the corresponding equations in (2.16) through (2.24), we obtain the following set of equations to model the whole PEB process:

$$\frac{\partial}{\partial t}v = k_2 u(1-v) \tag{2.26}$$

$$\frac{\partial}{\partial t}(u\omega) = -k_{loss} u\omega + \nabla \bullet (D_u \nabla u)\omega \tag{2.27}$$

$$D_u = D_{u0}\mathrm{Exp}(ah) \tag{2.28}$$

$$\frac{\partial}{\partial t}(w\omega) = k_1 k_2 u(1-v)\omega + \nabla \bullet (D_w \nabla w)\omega \tag{2.29}$$

$$\frac{\partial}{\partial t}(h\omega) = -\nabla \bullet (D_w \nabla w)\omega - k_3 h\omega \tag{2.30}$$

$$\frac{\partial}{\partial t}\omega = -k_4 k_3 h\omega \tag{2.31}$$

Since the volume element ω on the left-hand sides of the equations varies with time, we cannot move it out of the time derivatives and cancel with the ω on the right-hand sides. Thus

the volume shrinkage also affects the variation of the chemical (e.g., u, w, h) concentration in addition to diffusion and loss mechanisms. Consider a special case where the acid diffusion and loss terms are equal to zero, then equation (2.26) becomes

$$\frac{\partial}{\partial t}(u\omega)=0\text{, i.e., } u\omega=\text{constant.}$$

For example, if the volume shrinks by 50%, then the acid concentration doubles.

2.5.2 Initial and Boundary Conditions

The initial acid concentration can be obtained from the exposure dose distribution within the resist and photo-chemical reaction by equations (2.1) and (2.3). Again, we neglect the quenching effect, and repeat these equations below:

$$\mathrm{Dose}(z)=D_s\left(e^{-\alpha(d-z)}+|\tilde{r}|^2e^{-\alpha(d+z)}-2|\tilde{r}|e^{-\alpha d}\cos\left(\frac{4\pi nz}{\lambda}+\varphi_0\right)\right) \tag{2.32}$$

$$u(x,y,z)\big|_{t=0}=1-e^{-C\cdot\mathrm{Dose}(z)} \tag{2.33}$$

At the beginning of PEB there are no deprotection and no volatile group molecules, but there should be a certain amount of initial free volume h [20]:

$$v(x,y,z)\big|_{t=0}=0 \tag{2.34}$$

$$w(x,y,z)\big|_{t=0}=0 \tag{2.35}$$

$$h(x,y,z)\big|_{t=0}=h_0 \tag{2.36}$$

The boundary condition depends on the lithography process condition. For instance, assuming that there is no base contamination through the top surface, and no resist poisoning at the bottom, (i.e., there is no acid loss at the top and bottom boundary), we can write the acid boundary conditions as:

$$\frac{\partial}{\partial z}u(x,y,z)\bigg|_{z=0}=0 \tag{2.37}$$

$$\frac{\partial}{\partial z} u(x, y, z)\Big|_{z=d} = 0 \tag{2.38}$$

where x and y are directions parallel to the wafer surface, and z is the direction perpendicular to the surface and pointing upwards. These equations can also be modified to model T-topping and footing cases. Since the volatile group can diffuse very quickly through the top surface, we set its concentration there to be zero, and we assume that there is no loss of volatile group molecules at the resist bottom surface. So the boundary conditions are:

$$w(x, y, z)\big|_{z=d} = 0 \tag{2.39}$$

$$\frac{\partial}{\partial z} w(x, y, z)\Big|_{z=0} = 0 \tag{2.40}$$

2.6 Summary

In this chapter, we have proposed both static and dynamic physical models for DITL in CARs. These models will be validated using experimental data, and be used to extract the model parameters in Chapter 5. In the next chapter, we will implement the dynamic model using moving-boundary finite difference method in the one-dimensional case.

Chapter 3 Numerical Implementation of DITL Model with Moving-Boundary Finite Difference Method

3.1 Introduction

In chapter 2 we proposed a physically based dynamic model for DITL, based on a set of differential equations. In this chapter we first discretize the differential equations in one dimension perpendicular to the wafer surface, and employ a finite difference method to solve them. As the volume shrinks, the top boundary defined by the resist top surface, moves down. A moving boundary method is used in section 3.3 to accommodate this effect.

3.2 Finite Difference Formulation

We first implement our physically based dynamic model for DITL under flood exposure conditions, so we rewrite equations 2.25 through 2.30 in one dimension as follows:

$$\frac{\partial}{\partial t}v = k_2 u(1-v) \tag{3.1}$$

$$\frac{\partial}{\partial t}(u\omega) = -k_{loss}u\omega + \frac{\partial}{\partial z}\left(D_u \frac{\partial}{\partial z}u\right)\omega \tag{3.2}$$

$$D_u = D_{u0}e^{ah} \tag{3.3}$$

$$\frac{\partial}{\partial t}(w\omega) = k_1 k_2 u(1-v)\omega + \frac{\partial}{\partial z}\left(D_w \frac{\partial}{\partial z}w\right)\omega \tag{3.4}$$

$$\frac{\partial}{\partial t}(h\omega) = -\frac{\partial}{\partial z}\left(D_w \frac{\partial}{\partial z}w\right)\omega - k_3 h\omega \tag{3.5}$$

$$\frac{\partial}{\partial t}\omega = -k_4 k_3 h\omega \tag{3.6}$$

where z is the direction perpendicular to the wafer surface pointing upward, u, h and w are the concentration of acid, free volume and volatile group, respectively, normalized to the PAG length-concentration in number per unit length, and ω is the length element in the z direction.

Next we set the resist cross section and PEB time period as the simulation domain, all the variables such as u, v, w, and h are uniformly distributed in the x and y dimension, and they are functions of only z and PEB time t. We divide the z axis and the time into many discrete steps of the same size, and use the forward difference technique (explicit method) [21] in order to approximate the space and time derivatives of variable u numerically:

$$\frac{\partial}{\partial z}u(z,t) \cong \frac{1}{2\Delta z}\left(u(z+\Delta z,t) - u(z-\Delta z,t)\right) \tag{3.7}$$

$$\begin{aligned}\frac{\partial^2}{\partial z^2}u(z,t) &\cong \frac{1}{\Delta z}\left(\frac{\partial}{\partial z}u\left(z+\frac{1}{2}\Delta z,t\right) - \frac{\partial}{\partial z}u\left(z-\frac{1}{2}\Delta z,t\right)\right) \\ &\cong \frac{1}{(\Delta z)^2}\left(u(z+\Delta z,t) - 2u(z,t) + u(z-\Delta z,t)\right)\end{aligned} \tag{3.8}$$

$$\frac{\partial}{\partial t}u(z,t) \cong \frac{u(z,t+\Delta t) - u(z,t)}{\Delta t} \tag{3.9}$$

where Δz and Δt are the sizes of space step and time step, respectively. The space and time derivatives of variables w, h, v, ω (if applicable) can be discretized in the same way. Substituting them into equations 3.1 through 3.6, expanding the left-hand side of equations 3.2, 3.4 and 3.5, and replacing $\frac{\partial}{\partial t}\omega$ with equation 3.6, we can represent the values of variables u, v, w, h, ω at position z and time step $t+\Delta t$ as follows:

$$v(z,t+\Delta t) = v(z,t) + \Delta t\left[k_2 u(z,t)(1 - v(z,t))\right] \tag{3.10}$$

$$u(z,t+\Delta t)=u(z,t)+\Delta t\Big[-k_{loss}u(z,t)+k_4k_3h(z,t)u(z,t)$$
$$+a\cdot D_{u0}Exp(ah(z,t))\cdot\frac{1}{2\Delta z}(h(z+\Delta z,t)-h(z-\Delta z,t))$$
$$\cdot\frac{1}{2\Delta z}(u(z+\Delta z,t)-u(z-\Delta z,t)) \tag{3.11}$$
$$+D_{u0}Exp(ah(z,t))\cdot\frac{1}{(\Delta z)^2}(u(z+\Delta z,t)-2u(z,t)+u(z-\Delta z,t))\Big]$$

$$w(z,t+\Delta t)=w(z,t)+\Delta t\Big[k_1k_2u(z,t)(1-v(z,t))+k_4k_3h(z,t)w(z,t)$$
$$+D_w\frac{1}{(\Delta z)^2}(w(z+\Delta z,t)-2w(z,t)+w(z-\Delta z,t))\Big] \tag{3.12}$$

$$h(z,t+\Delta t)=h(z,t)+\Delta t\Big[-k_3h(z,t)+k_4k_3h(z,t)h(z,t)$$
$$-D_w\frac{1}{(\Delta z)^2}(w(z+\Delta z,t)-2w(z,t)+w(z-\Delta z,t))\Big] \tag{3.13}$$

$$\omega(z,t+\Delta t)=\omega(z,t)+\Delta t[-k_4k_3h(z,t)\omega(z,t)] \tag{3.14}$$

Starting from the initial and boundary conditions in section 2.5.2, as time progresses, we can calculate the values of variables during the entire PEB period.

The variable diffusion coefficient D makes this problem quite non-linear. To test the convergence of the program, we use the values of the parameters obtained in Chapter 5 (as listed in Table 5.5), and calculate the thickness loss for various space and space steps, as shown in Figure 3.1. Here we divide the space domain (resist thickness, which is 650 nm) into 50 to 600 steps, and use time steps of 3.0ms, 3.6ms, 4.5ms, 6.0ms, 9.0ms and 18.0ms. The curves for all the time steps converge asymptotically to 32.8 nm as the number of grids increases, except for the one simulated using 18ms time step, which is due to the stability criterion required when numerically solving diffusion problems using Forward Time Centered Space (FTCS) method [21].

For the basic diffusion equation derived from Fick's second law:

$$\frac{\partial}{\partial t}u=\frac{\partial}{\partial z}\left(D_u\frac{\partial}{\partial z}u\right), \tag{3.15}$$

the criterion for stability is given by [21]

$$\frac{2D\Delta t}{(\Delta x)^2} \leq 1. \tag{3.16}$$

However, there is no general rule of thumb to determine the stability of iteration when numerically implementing equations 3.10 through 3.14 using the FTCS method, we can only approximately use criterion (3.16) to have an idea about the situation. When time step is 18ms and the number of grids approaches 600 (i.e., the grid size is about 1nm), the left hand side of the inequality (3.16) is very close to 1, so the system is unstable and the curve does not converge as the number of grids increase.

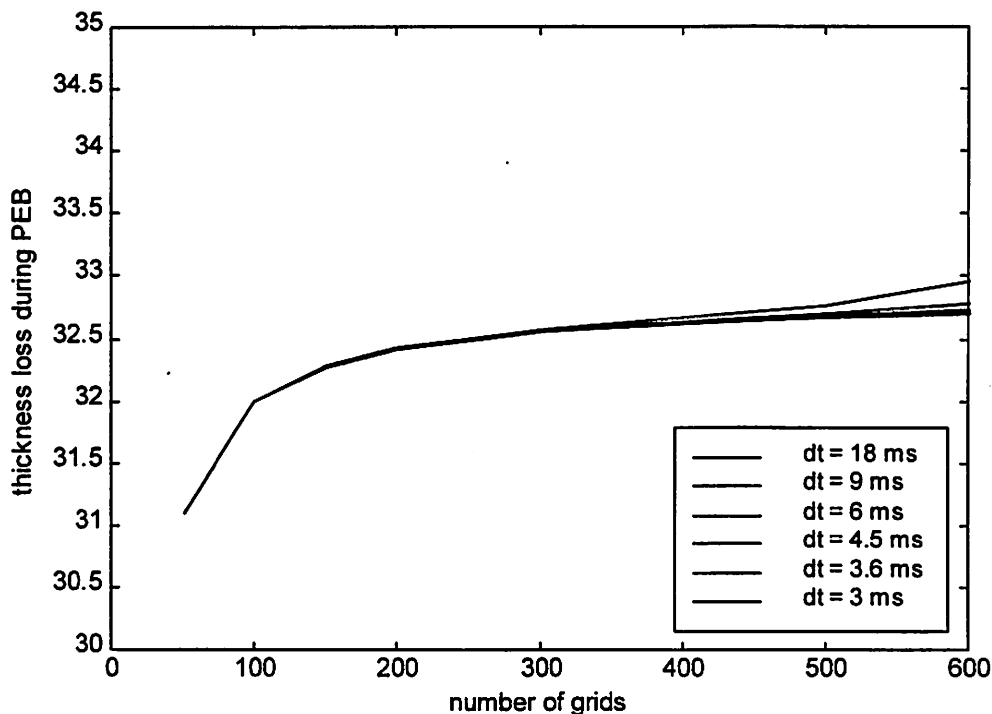

Figure 3.1 Convergence test results for various time steps

During the process of parameter extraction using adaptive simulated annealing, thousands of runs are needed, so we choose the size of time and space steps so that the simulation is stable and accurate enough. In this work, we use 200 space steps for total resist thickness of 650 nm and 5000 time steps for PEB time of 90 seconds. From Figure 3.1, we can see that this would induce about 0.5 nm error for the thickness loss, but this is good enough comparing to the experimental error (about 1.0 nm).

3.3 Moving Boundary Setup

We can see from equation 3.14 that the space domain step size Δz, which is represented by ω, shrinks after one time step. The grid sizes in space domain would become smaller and smaller, and the sizes of different steps would be quite different after a few time steps due to the non-uniform shrinkage. This invalidates our assumption of equal step size in space domain when we discretize the space derivatives in equations 3.7 and 3.8. So we need to adjust the space step to its original size after each time step.

As shown in Figure 3.2, at the beginning of time j (time = t), the distribution of a variable ξ (such as u, v, w, h, etc.) along z axis is plotted in solid curve $\xi(t)$. At the end of step j (time=t+Δt), due to chemical reaction, diffusion and volume shrinkage, not only the concentration at different z position changes, but also the whole curve shrinks along the z direction, as shown below. The concentrations of corresponding points at time t and time t+Δt are linked with dashed arrows.

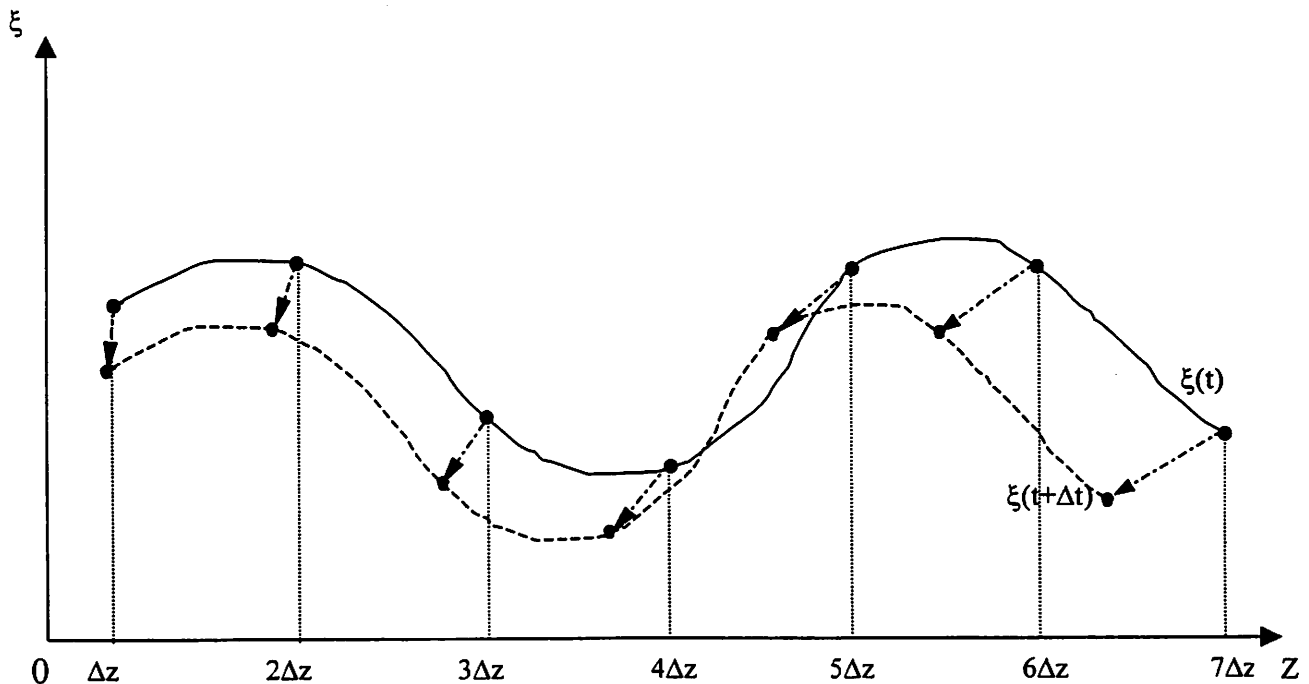

Figure 3.2. Space step size adjustment after each time step.

Therefore, at the end of step j, we obtain the concentration of variable ξ at positions marked by the dots on the dashed curve in Figure 3.1. Before starting the next time step, we interpolate using cubic splines [21] to get the concentration of variable ξ at position $k\Delta z$, (k=1, 2, ...). So the space steps are redefined at equal distances, except for the last step at the top surface of the resist, where only a fraction of Δz is left. A minor modification to equations 3.7 and 3.8 is needed to accommodate the unequal space step size. Furthermore, after a few time steps, the total amount of shrinkage in the z direction may be more than $k\Delta z$ (k=1, 2, ...), then the number of space steps will be N-k after adjustment, where N is the number of steps at the beginning of simulation. In this case, only these N-k steps are considered in the next iteration.

The method used above is called fixed finite-difference grid front-tracking method [37]. It is easy to extend this method to solve a two-dimensional moving boundary problem (Figure 3.3). As the iteration proceeds, at the end of each time step, we equalize the grid size, so that the

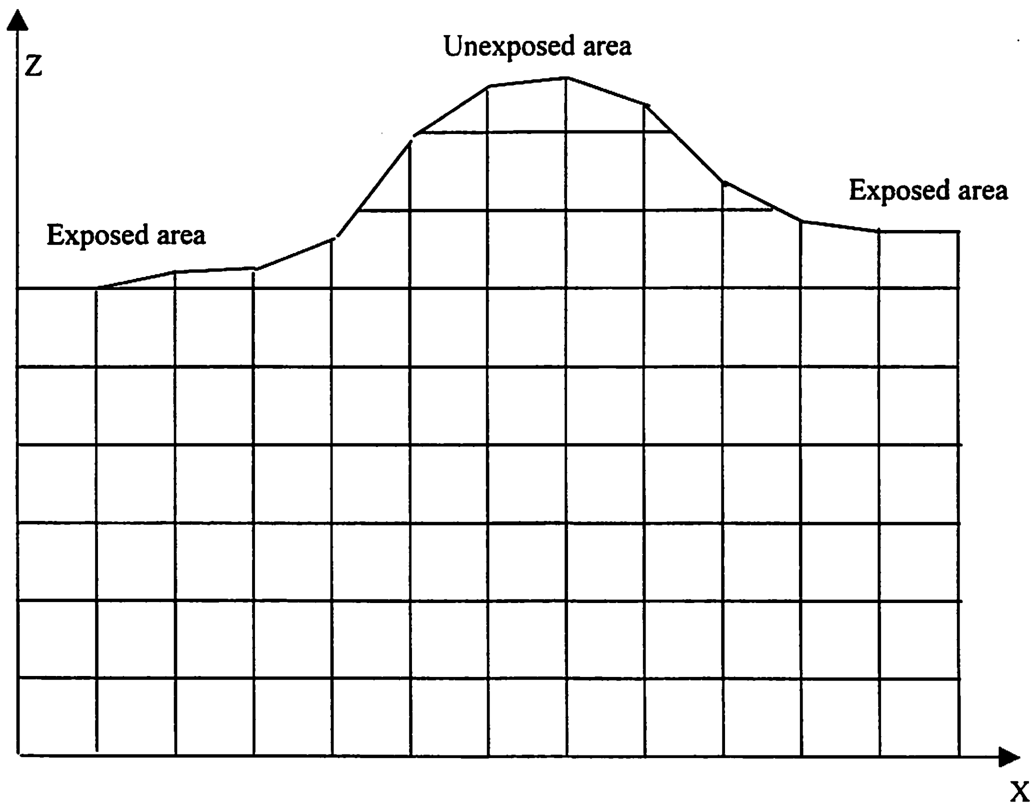

Figure 3.3 Two-dimensional fixed grid size method.

grid lines are still parallel to the coordinate axes. During this process the moving boundary is tracked by recording the sizes and indices of the top most grids along each vertical grid line.

Instead of equalizing the space step size at the end of each time step, we can also keep track of the grid sizes at different positions through out the simulation, and make some modifications to equations 3.7 and 3.8 when discretizing the derivatives. While this method works fine in the one-dimensional case, (maybe even easier than our previous method,) and it has been successfully implemented to solving moving-boundary problems using the finite element method [8], it is difficult to use with the finite difference method. As shown in Figure 3.4, after a

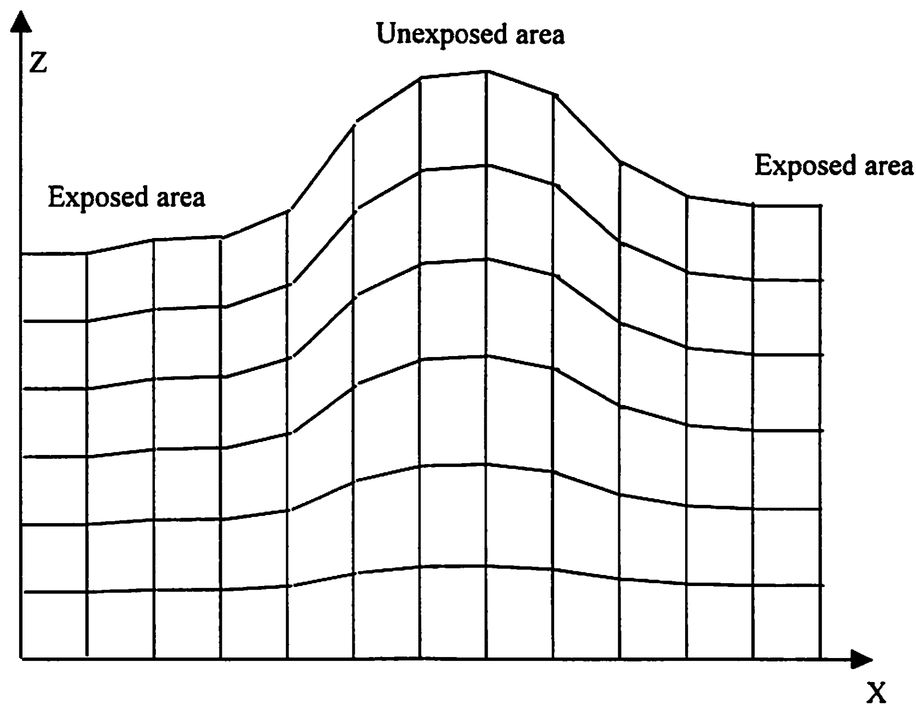

Figure 3.4. Grid-size tracking method for 2D moving-boundary problem.

few time steps, the grid lines in the x direction would no longer be parallel to the x axis due to non-uniform shrinkage. Therefore the discretizaion of space derivatives would no longer be as simple as before.

3.4 Summary

In this chapter we discretized the dynamic physical model for DITL using the finite difference method, then compared two methods for solving the moving-boundary problem. In the

next chapter, we will discuss the global optimization method, Adaptive Simulated Annealing (ASA), that will be used to extract the model parameters. Some practical issues about multilayer thin film thickness extraction will also be discussed.

Chapter 4 Adaptive Simulated Annealing and Multilayer Thin Film Thickness Extraction

4.1 Introduction

In chapters 2 and 3, resist models are proposed and implemented numerically to predict volume shrinkage and other process results given resist parameters. But in many cases, we need to solve the reverse problem, i.e., given the process metrology data, how can we extract the resist parameters? Since most of the models have either complicated solutions with no closed form reverse function, or no analytical solutions at all, some optimization technique must be employed to solve this non-linear multi-dimensional problem. Adaptive Simulated Annealing (ASA) is used for this problem, and is discussed in section 4.2.

In the experiment we do to validate our models and extract resist parameters, we need to measure the film thickness as it shrinks during PEB. For some resists, their refractive indices also change during this process, necessitating simultaneous extraction of both the thickness and the index. In section 4.3, we formulate the multilayer reflection problem, and use ASA for thickness and index extraction.

4.2 Adaptive Simulated Annealing

4.2.1 Global Minimization Problem

After developing the physical model, the resist parameter extraction problem can be viewed as a constrained minimization problem. Assuming that the model is correct, given a set of inputs, we need to minimize the deviation between the simulator output and the actual process output by tuning the model parameters. This can be formally specified as follows:

Define input vector $\bar{x}$ and parameter vector $\bar{p}$ as

$$\bar{x} = \begin{pmatrix} x_1 \\ x_2 \\ \vdots \\ x_n \end{pmatrix}, \qquad \bar{p} = \begin{pmatrix} p_1 \\ p_2 \\ \vdots \\ p_m \end{pmatrix}.$$

Given a multivariate function $f(\bar{x};\bar{p})$, the parameter constraint $C_p \in R^m$, a set of $\bar{x}$, and its corresponding output f_o, our goal is to solve the constrained minimization problem: $\mathrm{Min}\left(\| f(\bar{x};\bar{p}) - f_o \| : \bar{p} \in C_p\right)$, where $g(\bar{x};\bar{p}) \equiv \| f(\bar{x};\bar{p}) - f_o \|$ is the objective function.

As we have seen in previous chapters, the relation between the resist thickness loss during PEB and the resist and process parameters is modeled by a set of differential equations. It is likely that the objective function is multimodal, so a global minimization technique is needed to prevent the process from being trapped in local minima.

4.2.2 Simulated Annealing

Simulated annealing is a global optimization technique based on physical intuition about the physical annealing process. It was first used by Metropolis [22] as a Monte Carlo importance-sampling technique for doing large-dimensional path integrals arising in statistical physics problems. It was generalized by Kirkpatrick [23] to include a temperature schedule for efficient searching, and used in a variety of problems by other researchers [24] [25].

Simulated annealing uses three functional relationships [17]:

1. T_k: Schedule of "annealing", i.e., the "temperature" T at annealing-time step k.

2. $g(\bar{p}, T_k)$: Probability density of D-dimensional variable $\bar{p}$.

3. $h(\Delta E, T_k)$: Probability for acceptance of new state based on the previous state.

At each step during the annealing process, the "temperature" T_k is updated according to the annealing schedule. Next, a point $\bar{p}_k$ is sampled based on the probability density $g(\bar{p}, T_k)$, and the objective function (energy) is calculated and compared to that of the previous step to get $\Delta E = E_k - E_{accept}$, where E_{accept} is the energy of the last accepted state. Then the new state is either accepted or rejected with a probability $h(\Delta E, T_k)$.

In order to guarantee that the algorithm can statistically find a global minimum, the process should have the ergodicity property, i.e., any point $\bar{p} \in C_p$ can be sampled infinitely often in infinite annealing-steps. If the probability that $\bar{p}$ is sampled at step k is g_k, then it suffices to prove that the overall probability of not sampling point $\bar{p}$ for the annealing steps successive to k_0 is zero [26]:

$$\prod_{k=k_0}^{\infty}(1-g_k)=0 \tag{4.1}$$

This is satisfied if:

$$\sum_{k=k_0}^{\infty} g_k = \infty \tag{4.2}$$

Depending on different choices of T_k, $g(\bar{p}, T_k)$ and $h(\Delta E, T_k)$, there are various simulated annealing algorithms, such as *Fast Annealing* (FA) [27], *Adaptive Simulated annealing* (ASA) [28], *Parallel Annealing* (PA) [29], etc. As long as equation (4.2) is satisfied, the algorithm will find the global minimum statistically. We first discuss the "standard" Boltzmann Annealing.

The functional relationships are chosen as follows in the "standard" Boltzmann Annealing:

$$T_k = \frac{T_0}{\ln k} \tag{4.3}$$

$$g(\Delta\bar{p}, T_k) = (2\pi T_k)^{-D/2} \exp\left(-\|\Delta\bar{p}\|/(2T_k)\right) \tag{4.4}$$

$$h(\Delta E, T_k) = \begin{cases} \dfrac{1}{1+\exp(\Delta E / T_k)} \cong \exp(\Delta E / T_k) & \Delta E \geq 0 \\ 1 & \Delta E < 0 \end{cases} \tag{4.5}$$

where T_0 is a temperature value "large enough", D is the dimension of the parameter space, and $\Delta\bar{p} = \bar{p}_k - \bar{p}_{accept}$, which is the change from the last accepted state. Equation (4.5) is essentially the Boltzmann distribution contributing to the statistical mechanical partition function

of a multi-energy system, and equation (4.4) is chosen based on functional forms derived for some physical systems belonging to the class of Gaussian-Markovian systems. Given these functional relations, it has been proven that equation (4.2) is satisfied [30].

4.2.3 Adaptive Simulated Annealing

In a variety of practical problems some of the parameters can only span finite ranges, and there is no reason to let all the parameters "cool down" at the same rate, because the cost function may have different sensitivities to different parameters. Furthermore, the annealing schedule may be too slow, requiring too many runs for the optimization process to converge. ASA is one of the variations recently developed to accommodate these considerations.

In ASA, different parameters employ different cooling schedules to generate new state. The cooling schedule for parameter p_i is:

$$T_k^i = T_0^i \exp\left(-c^i \left(s_k^i\right)^{1/D}\right) \tag{4.6}$$

where T_0^i is the initial temperature for parameter p_i, s_k^i is the number of generations for p_i up to step k, c^i is the cooling scaling factor for T^i, and D is the parameter dimensionality . c^i can be set according to the sensitivity of the ith parameter. Given T_k^i and the finite range $p_i \in [A_i, B_i]$, the value of the ith parameter at time k is calculated from the last accepted state $p_i(k_{accept})$:

$$p_i(k) = p_i(k_{accept}) + y_i(B_i - A_i) \tag{4.7}$$

where $y_i \in [-1,1]$, and its probability density function is:

$$g_i(y_i, T^i) = \frac{1}{2(|y_i| + T^i)\ln(1 + 1/T^i)} \tag{4.8}$$

y_i can be generated from a uniformly distributed random number $u_i \in [0,1]$ with the following formula:

$$y_i = \mathrm{sgn}(u_i - 0.5) \cdot T^i \cdot [(1 + 1/T^i)^{|2u_i - 1|} - 1] \tag{4.9}$$

where the sign function sgn(·) is defined as

$$\mathrm{sgn}(x)=\begin{cases}1 & x>0\\ 0 & x=0\\ -1 & x<0\end{cases}$$

If the generated p_i falls outside of the range $[A_i, B_i]$, it is regenerated until it is within the range.

There is also a cooling schedule for cost, which is used to determine acceptance or rejection for the new state according to its cost:

$$T_{k,cost} = T_{0,cost}\exp\left(-c_{cost}k_{cost}^{1/D}\right) \tag{4.10}$$

where $T_{0,cost}$ is the initial cost temperature, k_{cost} is the number of acceptance, and c_{cost} is the cooling scaling factor for the acceptance function. Given T_{cost}, the probability function for acceptance of the new state is calculated as follows:

$$h(\Delta E, T_{cost}(k))=\begin{cases}\dfrac{1}{1+\exp(\Delta E/T_{cost})}\cong\exp(\Delta E/T_{cost}) & \Delta E\geq 0\\ 1 & \Delta E<0\end{cases} \tag{4.11}$$

From equations (4.6) through (4.11), we can see that the temperature cools down much faster than the "standard" Boltzmann annealing, and the algorithm can be adapted with different sensitivities for different parameters by adjusting the cooling scaling factor c_i.

4.3 Multilayer Thin Film Thickness Extraction

4.3.1 Multilayer Thin Film Reflection Formulation

In the experiment we do to validate our models and extract resist parameters, we use a broadband reflectometer to measure thin film thickness. The process can be modeled as a vertical incidence multilayer thin film reflection problem.

We start from the Fresnel reflection and transmission equations for perpendicular incidence. As shown in Figure 4.1, a plane electromagnetic wave is perpendicularly incident upon the interface between two media, whose complex refractive indices are $\tilde{\eta}_1$ and $\tilde{\eta}_2$,

respectively. ($\tilde{\eta}_i = n_i - jk_i$, $j = \sqrt{-1}$). In order to differentiate the incident and reflective light, in Figure 4.1 we draw the light beam in a slightly tilted angle. The same convention holds for other figures in this chapter. Then the electrical field reflection coefficient $\tilde{r}$ and the

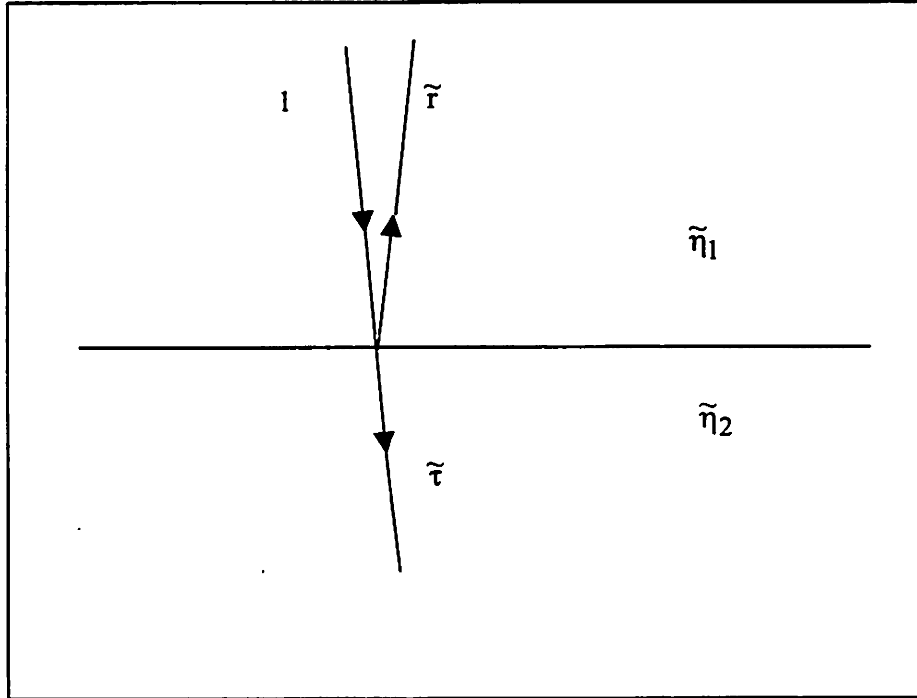

Figure 4.1. Incidence of plane electromagnetic wave upon two media interface.

transmission coefficient $\tilde{\tau}$ are:

$$\tilde{r} = \frac{\tilde{\eta}_2 - \tilde{\eta}_1}{\tilde{\eta}_2 + \tilde{\eta}_1} \quad (4.12)$$

$$\tilde{\tau} = \frac{2\tilde{\eta}_1}{\tilde{\eta}_2 + \tilde{\eta}_1} \quad (4.13)$$

Next, we derive the reflection from a single thin film layer. As shown in Figure 4.2, when light is incident upon the thin film, it not only reflects up from the top interface, but also bounces up and down within the film by the two interfaces, and partially transmits through each time it reflects at the interfaces. The overall reflection r is the summation of the reflections $\tilde{r}_0$, $\tilde{r}_1$, $\tilde{r}_2$, ..., which are given recursively below:

$$\tilde{r}_0 = \frac{\tilde{\eta}_2 - \tilde{\eta}_1}{\tilde{\eta}_2 + \tilde{\eta}_1} \quad (4.14)$$

$$\tilde{r}_1 = \frac{2\tilde{\eta}_1}{\tilde{\eta}_1 + \tilde{\eta}_2} \cdot e^{-j2\pi\frac{\tilde{\eta}_2 \cdot 2d}{\lambda_0}} \cdot \tilde{\gamma} \cdot \frac{2\tilde{\eta}_2}{\tilde{\eta}_1 + \tilde{\eta}_2} \quad (4.15)$$

$$\tilde{r}_i = \tilde{r}_{i-1} \cdot \frac{\tilde{\eta}_1 - \tilde{\eta}_2}{\tilde{\eta}_1 + \tilde{\eta}_2} \cdot e^{-j2\pi\frac{\tilde{\eta}_2 \cdot 2d}{\lambda_0}} \cdot \tilde{\gamma}, \quad i = 2, \ 3, \ \cdots \quad (4.16)$$

where d is the thin film thickness, λ_0 is the light wavelength in vacuum, and $\tilde{\gamma}$ is the reflection at the lower interface. So the total reflection coefficient $\tilde{r}$ can be calculated from the sum of the

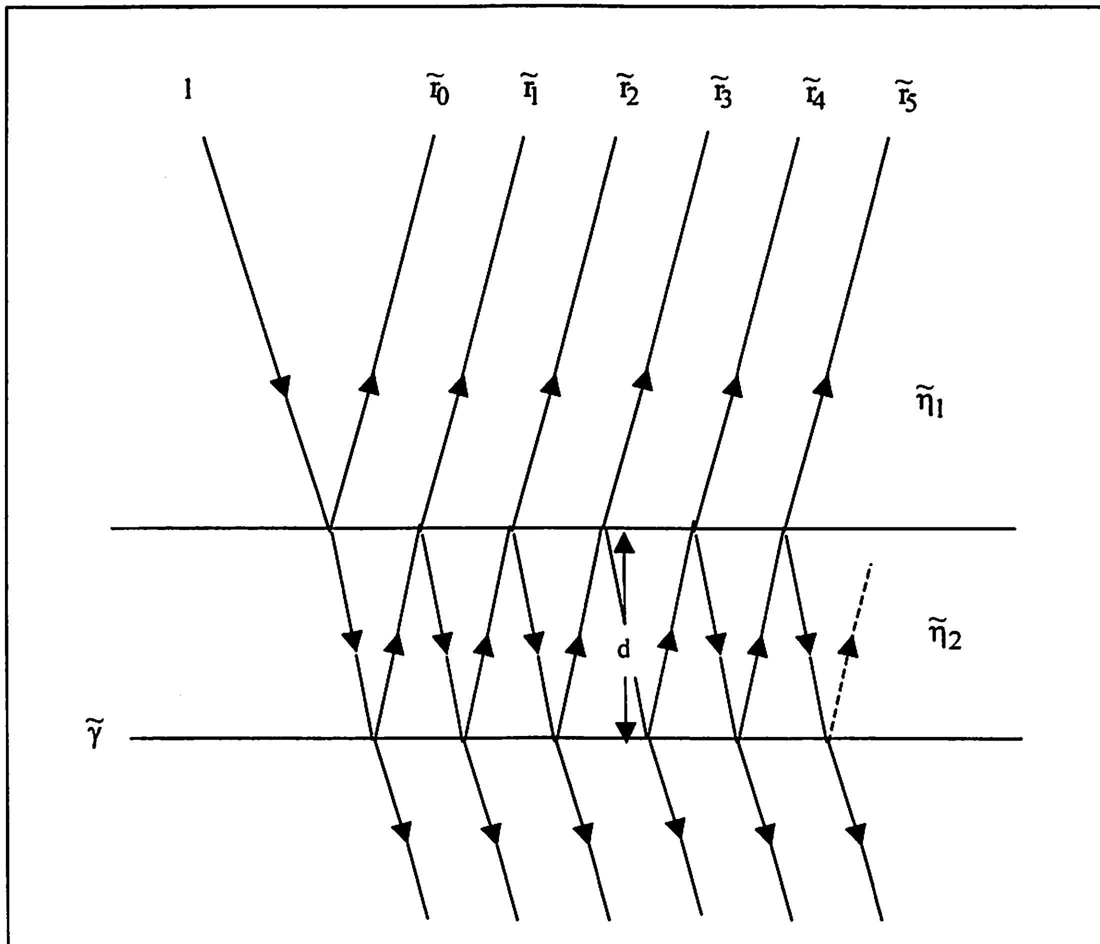

Figure 4.2. Reflection of plane electromagnetic wave from a single layer of thin film.

infinite series:

$$\tilde{r} = \sum_{i=0}^{\infty} \tilde{r}_i = \frac{\tilde{\eta}_2 - \tilde{\eta}_1}{\tilde{\eta}_2 + \tilde{\eta}_1} + \frac{2\tilde{\eta}_1}{\tilde{\eta}_1 + \tilde{\eta}_2} \cdot \frac{2\tilde{\eta}_2}{\tilde{\eta}_1 + \tilde{\eta}_2} \cdot \frac{\tilde{\gamma}}{\frac{\tilde{\eta}_2 - \tilde{\eta}_1}{\tilde{\eta}_2 + \tilde{\eta}_1} \cdot \tilde{\gamma} + e^{j2\pi \frac{\tilde{\eta}_2 \cdot 2d}{\lambda_0}}} \tag{4.17}$$

We can write the reflection from the single layer film as a function

$$\tilde{r} = \tilde{r}(\tilde{\eta}_1, \tilde{\eta}_2, d, \tilde{\gamma}, \lambda_0) \tag{4.18}$$

In the case of multilayer thin film, given the thickness d_1, d_2, ..., d_k, and the refractive indices of each layer $\tilde{\eta}_1$, $\tilde{\eta}_2$, ..., $\tilde{\eta}_1$, $\tilde{\eta}_0$ for substrate, and $\tilde{\eta}_{k+1}$ for incident medium, we can derive the reflection recursively from bottom to top, as shown by the pseudo-code in Figure 4.3. The final reflection from the multilayer system can be written as:

$$\tilde{r} = \tilde{r}(\tilde{\eta}_0, \tilde{\eta}_1, \cdots, \tilde{\eta}_k, \tilde{\eta}_{k+1}; d_1, d_2, \cdots, d_k; \lambda_0) \tag{4.19}$$

and the intensity reflectivity is

$$R = |\tilde{r}|^2 \tag{4.20}$$

```
Begin
        γ̃ = (η̃0 − η̃1) / (η̃0 + η̃1)
        for i=1 to k
                γ̃ = r̃(η̃i+1, η̃i, di, γ̃, λ0) according to equation (4.18)
        next i
        r̃ = γ̃
End
```

Figure 4.3. Pseudo-code for multilayer thin film reflection.

4.3.2 Multilayer Thin Film Thickness Extraction Using ASA

As we can see from equations (4.19) and (4.20), given a multilayer thin film system, the reflectance is a function of wavelength λ_0. So, if we can measure the intensity of the reflection at multiple wavelengths, the number of measurements is more than the number of unknowns, and these equations are linearly independent, we can solve the unknown system parameters. This is the basic principle of reflectometry.

The index $\tilde{\eta} = n - jk$ is a function of light wavelength λ, but we can model the dispersion behavior using some dispersion formulae with a few parameters over a certain wavelength range. The Cauchy model we use consists of two simple empirical equations in the following form:

$$n(\lambda) = A_c + \frac{B_c}{\lambda^2} + \frac{C_c}{\lambda^4} \tag{4.15}$$

$$k(\lambda) = \frac{D_c}{\lambda} + \frac{E_c}{\lambda^3} + \frac{F_c}{\lambda^5} \tag{4.16}$$

Although many physically sensible models have been developed [31] [32] [33] [34], they are complicated and do not show significant advantage over Cauchy model at the wavelength range we use (500 nm ~ 800 nm).

In the experiment we do to validate our DITL model, we use the Inspector 800 reflectometer provided by SC Technologies. Although the SC system can collect and analyze data at a very high speed (as many as 10 measurements per second), the reflective indices of the

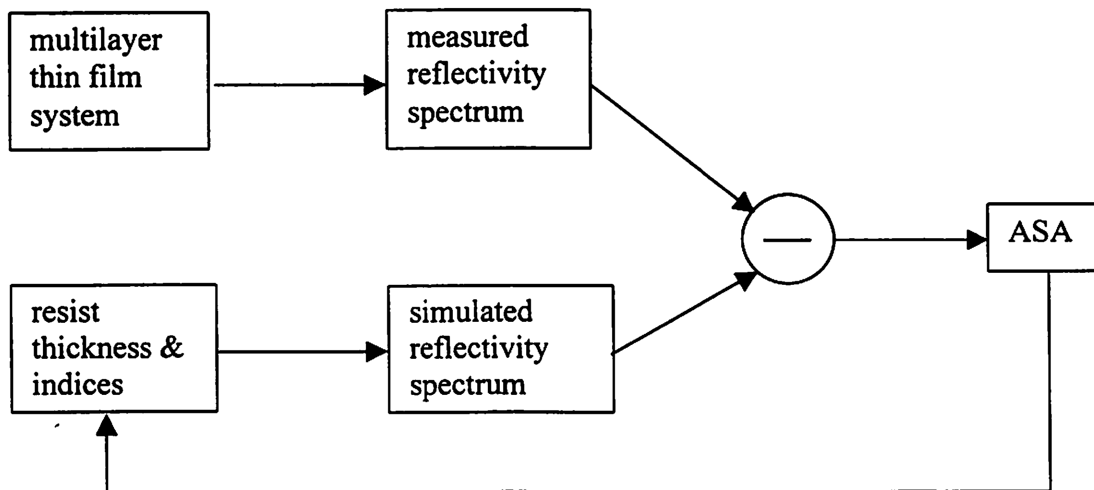

Figure 4.4. Resist index and thickness extraction framework.

film stack must be provided first. However, for some of the resists we test, the indices keep changing during the PEB process, which necessitates simultaneous extraction of thickness and index. We use ASA [35] as optimization engine to do the extraction, as shown in Figure 4.4. First, the reflected spectrum is measured using the SC reflectometer, then during the extraction process, a set of resist thickness and Cauchy coefficients are generated by ASA, and used to calculate the reflectivity. It is compared with the experiment spectrum, and the new set of parameters is accepted or rejected depending on ASA. The iteration proceeds until the cost is "small enough"[1].

4.4 Summary

In this chapter, we discussed the algorithm of the optimization engine, ASA, that we used for parameter extraction, and solved the multilayer thin film thickness extraction problem. In the next chapter, we will present the experimental data and parameter extraction results for both static and dynamic models.

[1] When we say the error is "small enough" in this thesis, we use two criteria. One is the Root-Mean-Square (RMS) of the error, i.e., when the RMS is smaller than the measurement noise, we say the error is "small enough". The other is R-Square. When the R-Square correlation between the simulation and the data is larger than 0.95, we say that the error is "small enough".

Chapter 5 Experimental Setup and Parameter Extraction Results

5.1 Introduction

In this chapter we show and discuss experimental results. First, we propose a parameter extraction framework, and then discuss some practical experimental issues. Next we extract some resist parameters using the static process models. Finally, additional resist parameters are extracted with the dynamic DITL model, where parameter values extracted with the static models are used to reduce the problem dimensionality.

5.2 Parameter Extraction Framework

As discussed in chapter 2, most of the resist models (both static and dynamic) present multidimensional, nonlinear problems, which can be written in the form:

$$f = f(\bar{x};\bar{p}) \tag{5.1}$$

where $\bar{x}$ is the process input vector, and $\bar{p}$ is the model parameter vector. For example, for the quencher reaction model equation (2.15), $\bar{x} = [t,[Acid]_0]^T$, $\bar{p} = [k_\alpha,[Q]_0,k_{amp}]^T$. Adaptive Simulated Annealing [26] is extensively used in solving these problems to extract model parameters $\bar{p}$ by minimizing the deviation between the model and the process output.

The general parameter extraction framework is shown in Figure 5.1. First experiment is designed and output data f_o is collected for an input vector $\bar{x}$. Then during the optimization process, at each step k, a model parameter vector $\bar{p}_k$ is generated by the ASA engine, fed into the function $f(\bar{x};\bar{p}_k)$ together with $\bar{x}$, and the simulation output f_k is calculated. Based on the deviation between f_k and f_o as well as the ASA acceptance rule, the parameter vector $\bar{p}_k$ is accepted or rejected. The iteration continues until the cost is small enough.

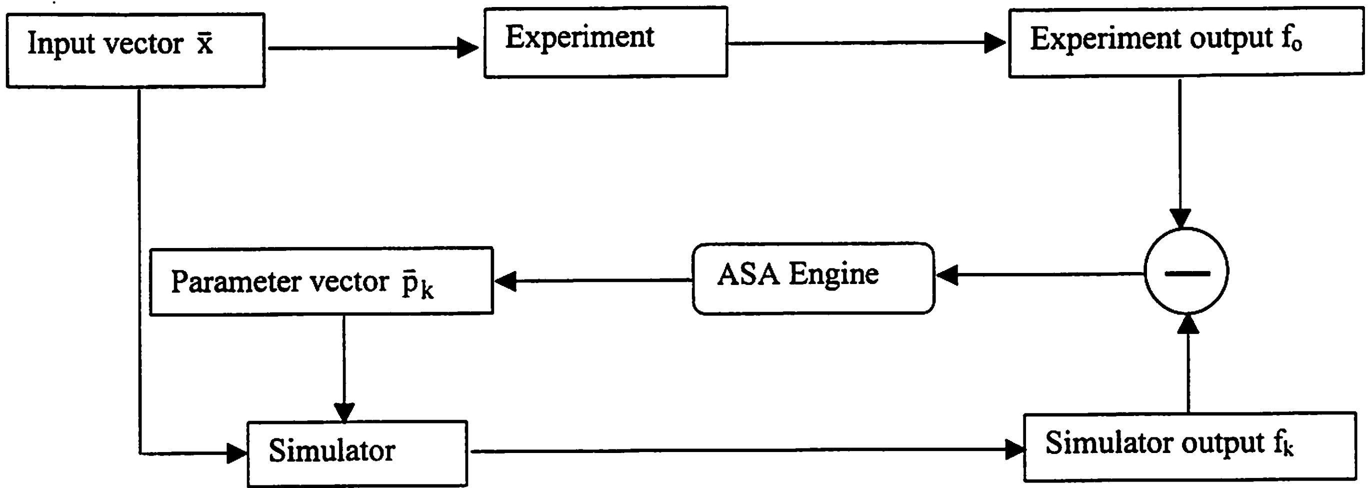

Figure 5.1. General parameter extraction framework.

5.3 Experiment Setup

5.3.1 Experiment Design

We did an experiment on Shipley's UV5 and Clariant's AZ2549 resists to validate our models proposed in chapter 2, and extract model parameters. The experiment on UV5 was done by Nickhil Jakatdar and co-workers at Advanced Micro Devices during the summer of 1997. After PEB, *Fourier Transform Infrared Spectroscopy* (FTIR) was employed to measure the photoacid-induced deprotection of the resist, and an ellipsometer was used to measure deprotection induced thickness loss. Then a poor man's DRM experiment was done to quantify dissolution rate.

The experiment on AZ2549 was done by the author together with Nickhil Jakatdar, Steve Hu and John Lin in the Berkeley MicroLab in the winter of 1998. Designed experiments were done to collect as much data as possible to validate both the static process model and the dynamic DITL model using the same set of wafers.

The resist was first spun on the wafer and softbaked at 120 °C for 90 seconds. The maximum field size of the DUV stepper in MicroLab is about 2mm by 5mm. Since it can only step in one direction, eight flood exposures of different doses were made along the diameter on

each of the ten wafers used. Because AZ2549 is a resist still being developed, we did not get much information about the parameters conventionally provided by the vendor, such as refractive index, dose-to-clear, etc. So we first measured dose-to-clear for normal develop time with one wafer, then exposed the remaining nine wafers with doses centered at dose-to-clear and 2 mJ/cm^2 step-size. Next, the wafers were baked at 110 °C for 90 seconds, and developed at different development times to measure dissolution rate and employ the Poor Man's DRM technique. The experimental conditions are listed in Table 5.1.

Table 5.1 Experimental Conditions for Resist AZ 2549

softbake temperature	120 °C
softbake time	90 seconds
exposure dose	10 ~ 24, step of 2 mJ/cm^2
PEB temperature	110 °C
PEB time	90 seconds
develop time	5, 10, 15, 25, 35, 45, 55, 70, 90 seconds

At the end of each process step (softbake, exposure, PEB, and development) as well as during PEB, the reflectivity spectrum was measured using the SC Inspector, and the resist thickness was extracted with the method described in section 5.3.2.

5.3.2 Resist Thickness Extraction

All through the experiment on resist AZ2549, the SC Inspector was used to measure reflectivity. The inspector has been designed for in-line measurement of the thickness and the absolute reflectivity of semi-transparent thin films. As mentioned in chapter 4, the tool requires the resist refractive index in order to measure thickness. However, the index of AZ2549 keeps changing at each process step and during PEB, so we can only use the SC tool to measure reflectivity, and use ASA as the optimization engine to extract thickness.

The reflectivity spectrum ranges from 500 nm to 800 nm. The film stack is resist on native oxide on silicon. In this range, the absorption of the light for both resist and oxide is negligible, so the index has only a real part. There were seven parameters to be extracted, three Cauchy parameters (A_r, B_r, C_r) for the resist index, two Cauchy parameters (A_o, B_o) for oxide, and resist and oxide thicknesses (d_r, d_o). To extract parameters in a seven-dimensional space for each measurement requires too many function evaluations, so we did it in two steps. Since the oxide thickness and index did not change during the process, we first chose one spectrum for each wafer, extracted all seven parameters with 40,000 evaluations. Then for the remaining spectra measured on the same wafer, we fixed A_o, B_o and d_o, extracting only resist Cauchy parameters and thickness.

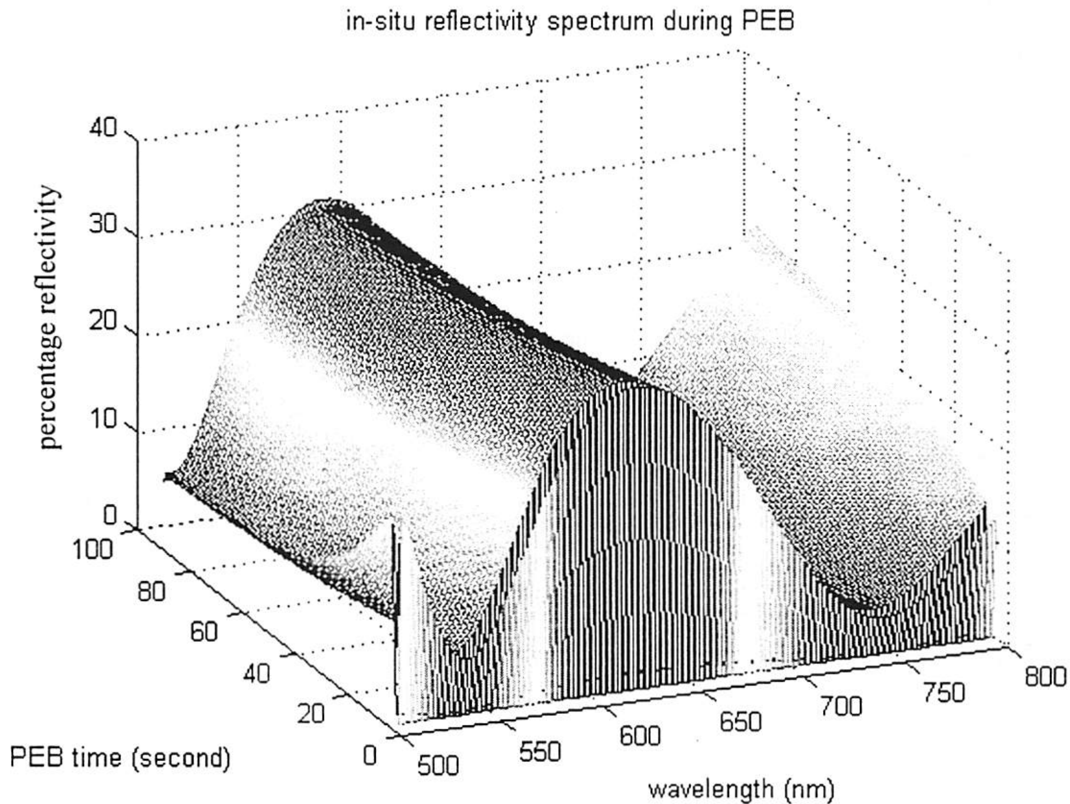

Figure 5.2. In-situ reflectivity spectrum during PEB.

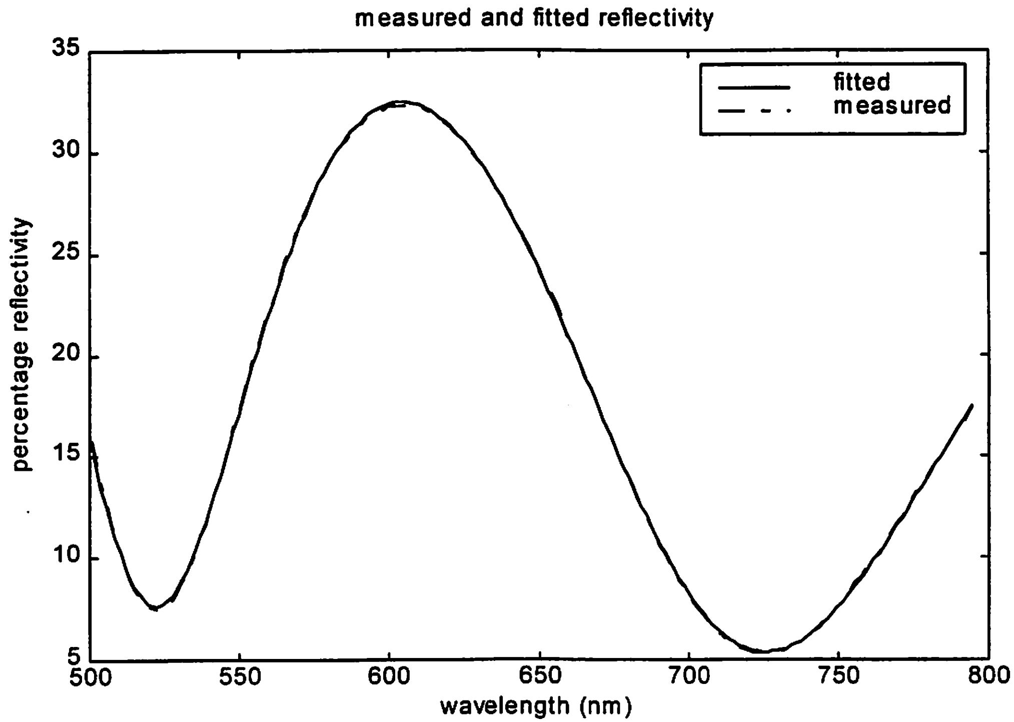

Figure 5.3. Comparison of measured and fitted reflectivity at 17th second.

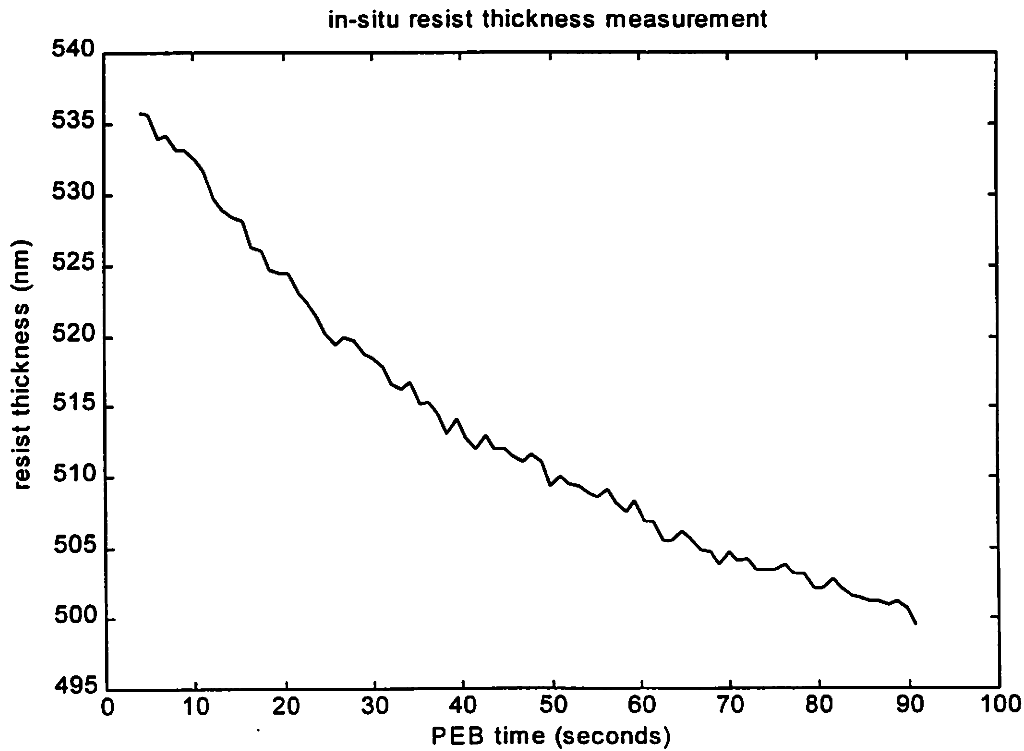

Figure 5.4. Resist thickness change during PEB.

For example, for wafer number 19, we measured the reflectivity spectrum during PEB *in*

situ, as shown in Figure 5.2. Because the exposed field size on the wafer is very small (2mm by 5mm), although the measurements started as soon as the wafer was placed on the bake plate, it took 3 to 5 seconds to properly position the light spot at the center of the field. This causes the sharp spikes at the first 5 seconds in the spectrum.

Picking up a low noise spectrum from Figure 5.2 (we choose the spectrum at the 17th second), we can extract all of the seven parameters accurately with a large number of runs. The measured and fitted spectrum is plotted in Figure 5.3. The root-mean-error is about 0.001.

Next the oxide thickness and index are fixed, and the resist thickness is extracted from the remaining spectra. The resist thickness change during PEB is plotted in Figure 5.4.

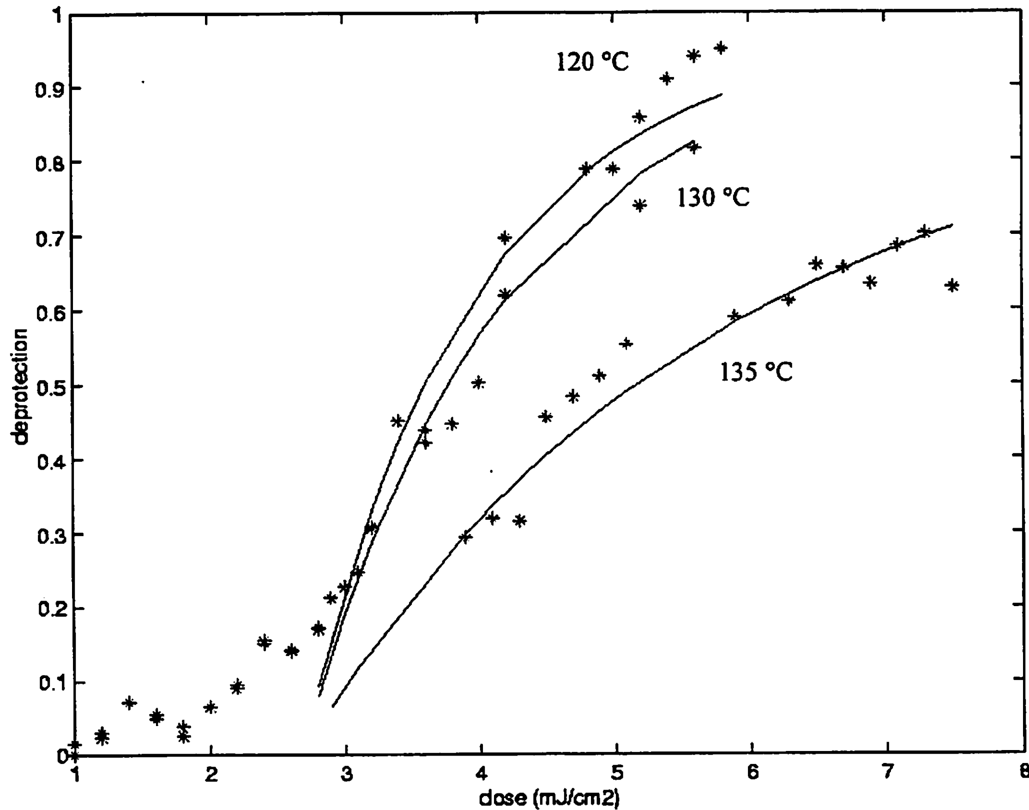

Figure 5.5. Fitting experiment data with reduced effective dose model.

5.4 Parameter Extraction with Static Process Models

5.4.1 Validation of Static Models for Deprotection Considering the Quenching Effect

In chapter 2 we found from Figure 2.3 that the amount of deprotection starts ramping up after a certain dose, and proposed that this is due to the effect of the quencher during PEB. In section 2.4.1 we first modeled this effect by using the difference between the dose coupled into the resist and a fixed amount of effective quenching dose as an effective dose that generates acid during PEB. I.e., substitute equation 2.9 into 2.4 to obtain the deprotection. With this model, we can fit the experiment data as shown in Figure 5.5. We can see that this model can describe the deprotection behavior fairly well for dosage above 3 mJ/cm^2. Below this dosage, the deprotection curve simply cuts off the dose-axis at about 2.75 mJ/cm^2, which is the effective quencher dose.

In order to model the deprotection process across the whole dosage range, we proposed the quencher reaction model (equation 2.15) in section 2.4.2, which models the actual quencher-acid reaction during PEB. We can easily fit this model to the UV5 deprotection-dose data at a PEB temperature of 135 °C. As we can see in Figure 5.6, this curve can fit the slow ramping up at low dosage very well.

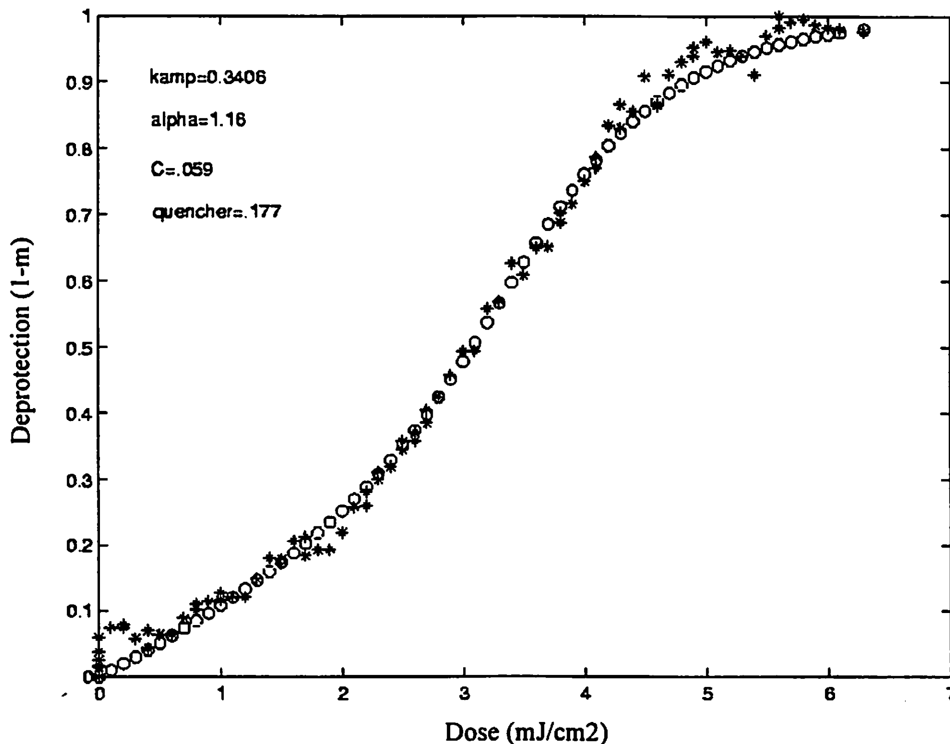

Figure 5.6. Fitting UV5 experiment data with quencher reaction model at 135 °C(Circles denotes simulated results, stars denotes experiment data).

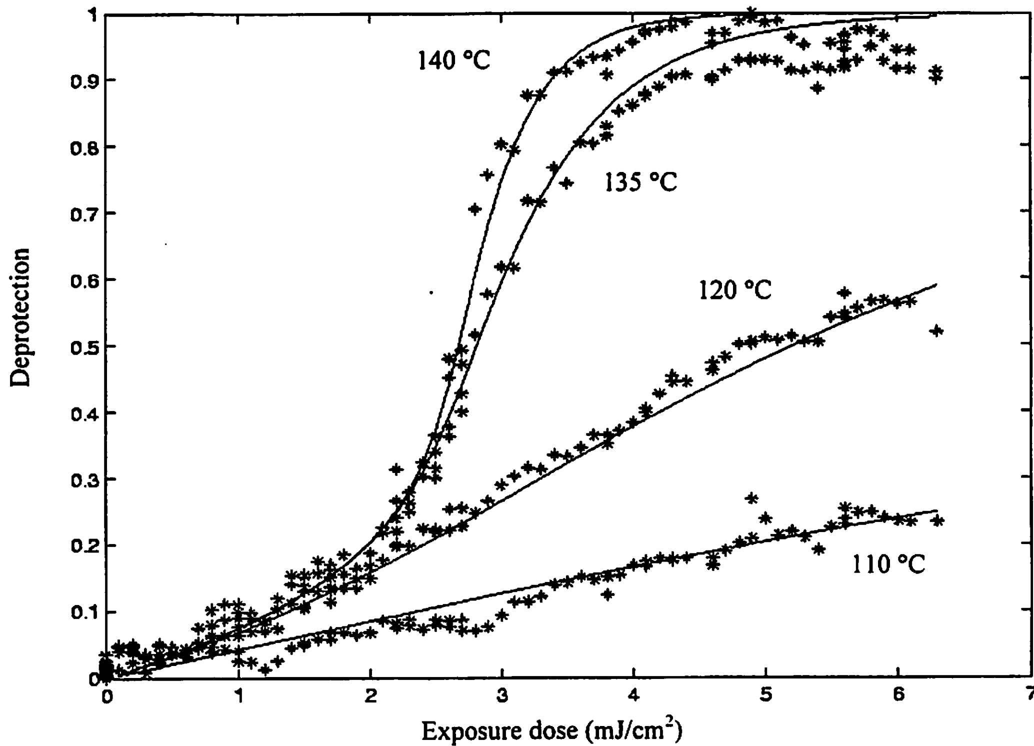

Figure 5.7 Static model fitting experimental data for UV5 at different PEB temperature.

5.4.2 Parameter Extraction with Static Process Models

As we have seen in chapter 2, there are more than 10 parameters in the resist models that describe exposure, PEB and development. We can extract these parameters in such a high-dimension non-linear space by divide-and-conquer. In this section, we extract some parameters from the static PEB and develop models, then use them to further extract other parameters in dynamic DITL model.

The quencher reaction PEB model (equation 2.15) is used to extract the Dill's C parameter, the acid amplification factor k_{amp}, the neutralization reaction coefficient k_{α}, and the relative quencher concentration $[Q]_0$. The experiment data and the fitted curves for resists UV5 at 135 °C and AZ 2549 at 110 °C are plotted in Figure 5.7 and Figure 5.8, respectively, and the extracted parameter values are shown in Table 5.2.

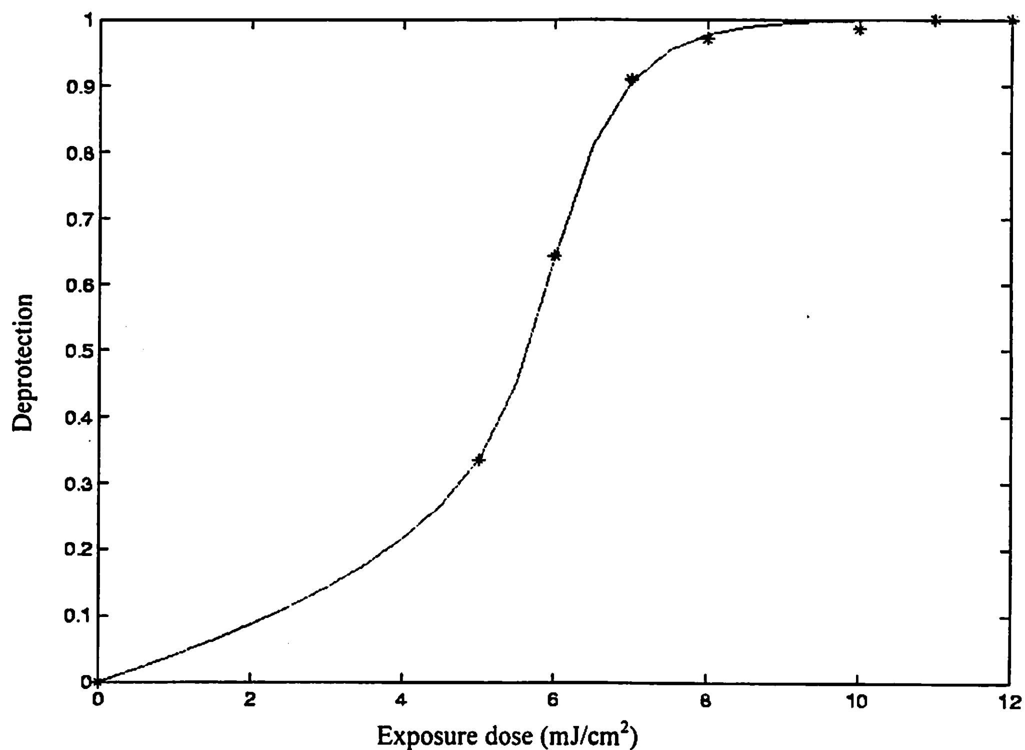

Figure 5.8 Static model fitting experimental data for AZ2549 at PEB temperature 110 °C.

Table 5.2 Results of Parameter Extraction using Static PEB Models at one temperature only

Parameter	UV5 (135 °C only)	AZ 2549 (110 °C only)
C (cm^2/mJ)	0.059	0.0798
$k_{amp}[PAG]_0$ (sec^{-1})	0.3406	0.3673
$k_{\alpha}[PAG]_0$ (sec^{-1})	1.16	2.06
$\frac{[Q]_0}{[PAG]_0}$	0.177	0.367

Table 5.3 Parameter extraction of UV5 for all temperatures

Parameter	$\ln(A_{amp}[PAG]_0)$ (sec^{-1})	E_{amp} ($kcal*mol^{-1}$)	$\ln(A_\alpha[PAG]_0)$ (sec^{-1})	E_α ($kcal*mol^{-1}$)	C (cm^2/mJ)	$\frac{[Q]_0}{[PAG]_0}$
Values	47.44	39.33	48.59	38.73	0.0531	0.1293

Since the pre-exponent parameters (A_{amp} and A_α) and the activation energies (E_{amp} and E_α) confound with each other at a fixed PEB temperature, we extract the UV5 parameter values using the data for all the PEB temperatures. The result is listed in Table 5.3. The parameter values provided by the resist vendor are: $\ln(A_{amp}[PAG]_0) = 47.818\ sec^{-1}$, $E_{amp} = 39.623\ kcal*mol^{-1}$, $C = 0.0510\ cm^2/mJ$, $\frac{[Q]_0}{[PAG]_0} = 0.150$. We can see that the extracted parameter values in Table 5.3 are fairly close to the values given by the resist vendor, which were obtained by different methods. Currently no resist vendors model the dynamic quenching reaction phenomenon, but we can still approximately check the validity of the neutralization reaction coefficient k_α as follows. During the quenching process, the acid loss rate is $k_\alpha*[Q]$, the maximum acid loss rate is $k_\alpha*[Q]_0 = 0.3143\ sec^{-1}$ at 135 °C, and the minimum acid loss rate is close to zero. The average acid loss rate k_{loss} given by the resist vendor is $0.0407\ sec^{-1}$ at 135 °C, which falls within the interval we calculated above.

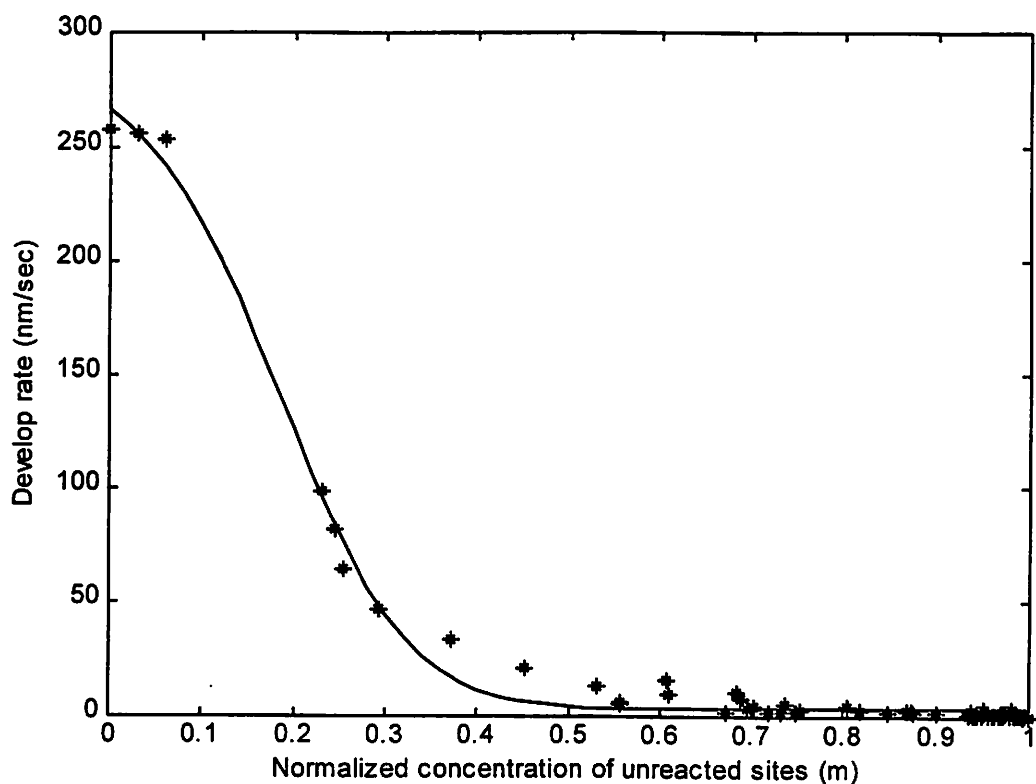

Figure 5.9 Develop rate versus the normalized concentration of unreacted sites for UV5

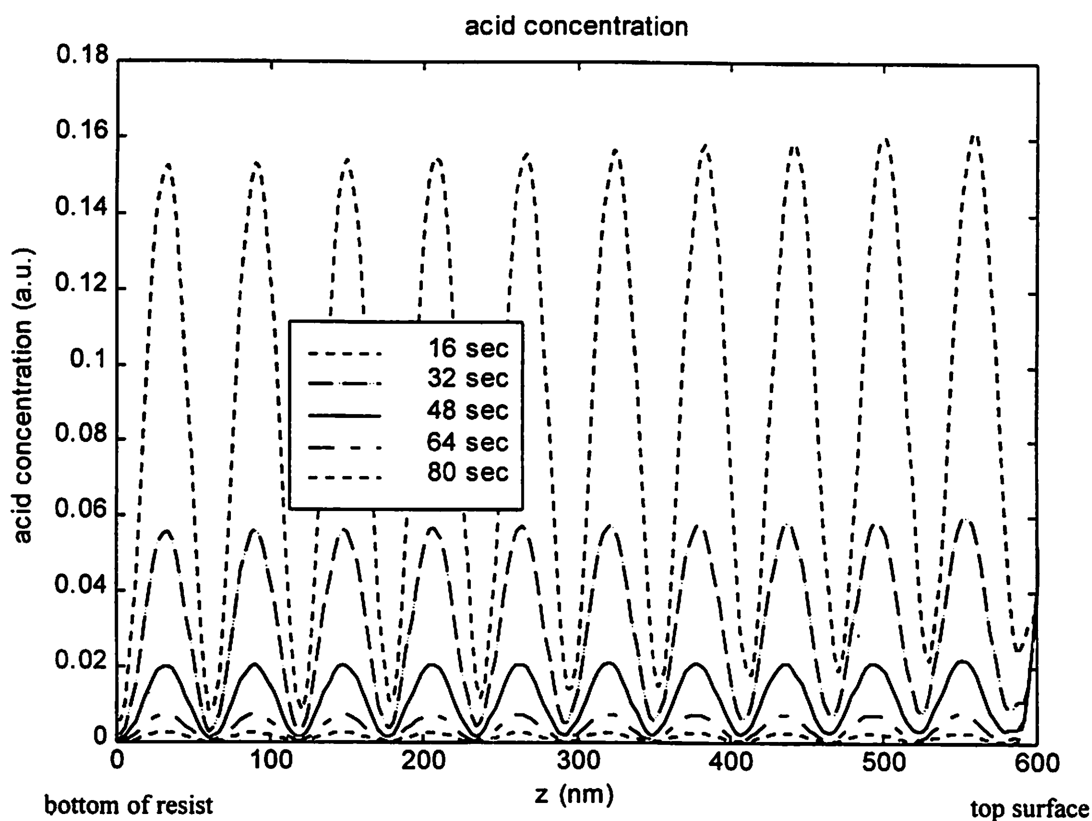

Figure 5.10 Acid concentration at different time steps during PEB for UV5.

The Mack develop model (equations 2.7 and 2.8) is used to extract the parameters for the develop process. There are 4 parameters (R_{max}, R_{min}, m_{th} and n) in the model. It took about 5 minutes to reduce the mean-square-error to 5nm/sec for develop rate after 30000 runs using ASA on a 350 MHz P-II PC. The extracted parameter values are listed in Table 5.4, and the experimental data collected using Poor Man's DRM (stars) and the model curve (solid line) plotted from the extracted parameters are shown in Figure 5.9. The parameter values extracted are similar to those obtained from alternate methods.

Table 5.4 Develop Parameter Extraction Results for UV5

Parameter	R_{max} (nm/sec)	R_{min} (nm/sec)	n_s	m_{th}
Value	263.6	3.099	11.04	0.188

5.5 Parameter Extraction with Dynamic DITL Model

5.5.1 Dynamic DITL Model Validation

A C++ program was written to implement the dynamic DITL model proposed in chapter 2. For both UV5 and AZ 2549, the resist thickness is about 650 nm, and the PEB time is 90 seconds. We divide the space domain (along the depth of the resist layer) into 200 grids, and the time domain into 5000 steps. It takes about 90 seconds to finish the simulation on a 350 MHz P-II PC.

Using the program, we cannot only calculate the volume shrinkage during PEB, but also find out the change of the chemical concentrations, such as acid, deprotected sites, etc., in the resist, as the reaction proceeds. Figures 5.10 to 5.13 show the distribution of acid concentration, deprotection, volatile group concentration, and free volume concentration at five different time steps for UV5. As expected, the acid concentration gets more uniform as PEB progresses, and the magnitude decreases due to the quenching effect. As a result, about half of the total deprotection and volatile group generation is done during the first 20 seconds. The free volume concentration starts from 0.08 (see next section) at the beginning of PEB, increases to 0.28 in the first 16 seconds, then keeps decreasing until the end of PEB. This is because during the first 16 seconds, the free volume generation is faster than relaxation due to the high acid concentration. After that the acid generation slows down, and the relaxation dominates.

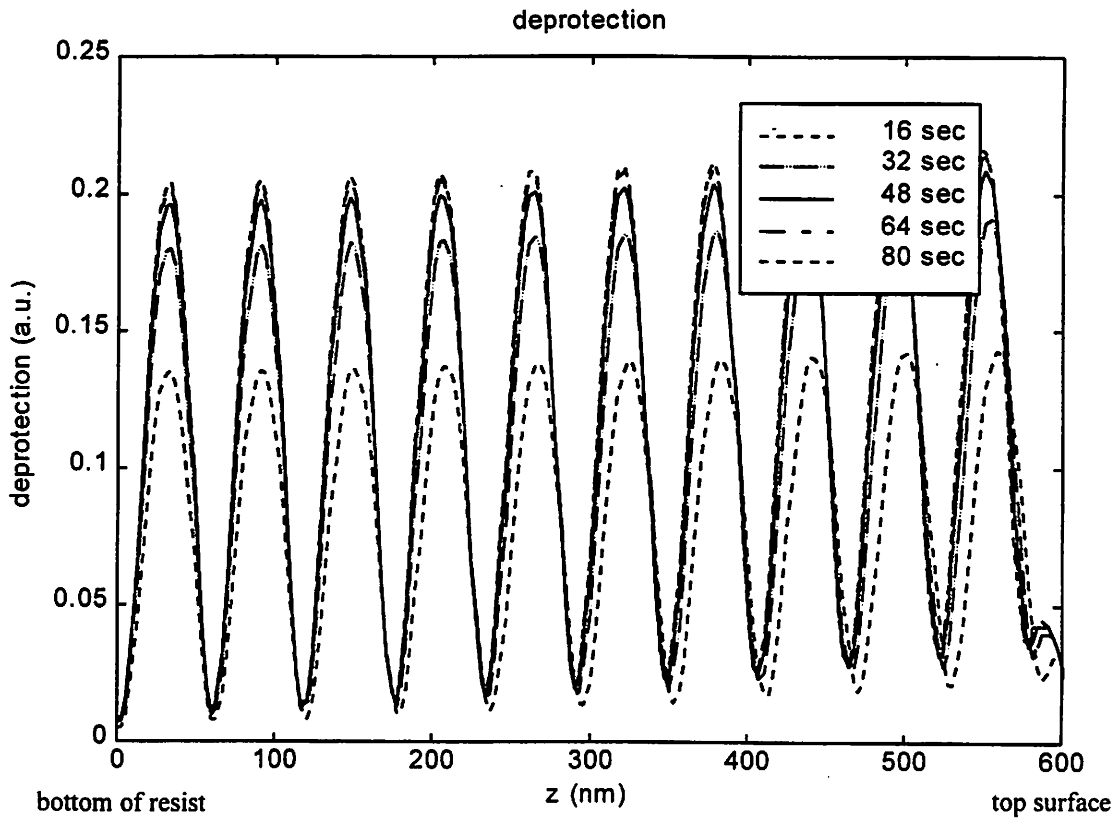

bottom of resist z (nm) top surface

Figure 5.11 Percentage deprotection at different time steps during PEB for UV5.

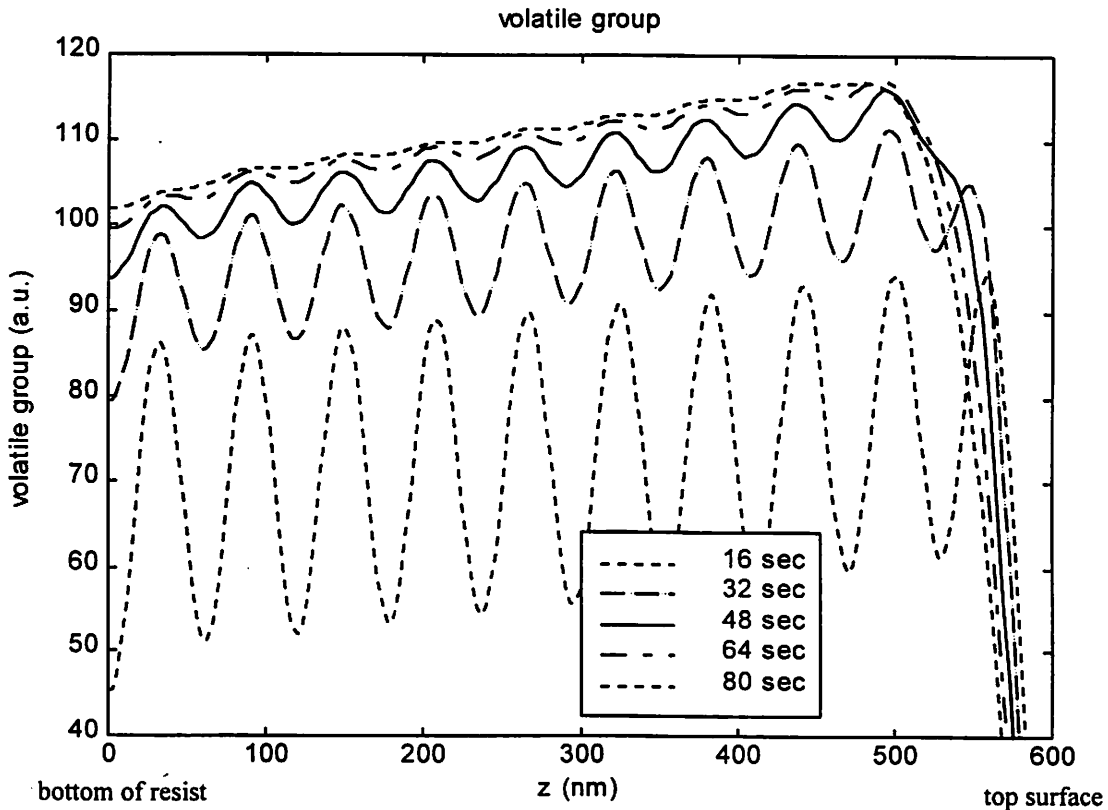

bottom of resist z (nm) top surface

Figure 5.12 Volatile group concentration at different time steps during PEB for UV5.

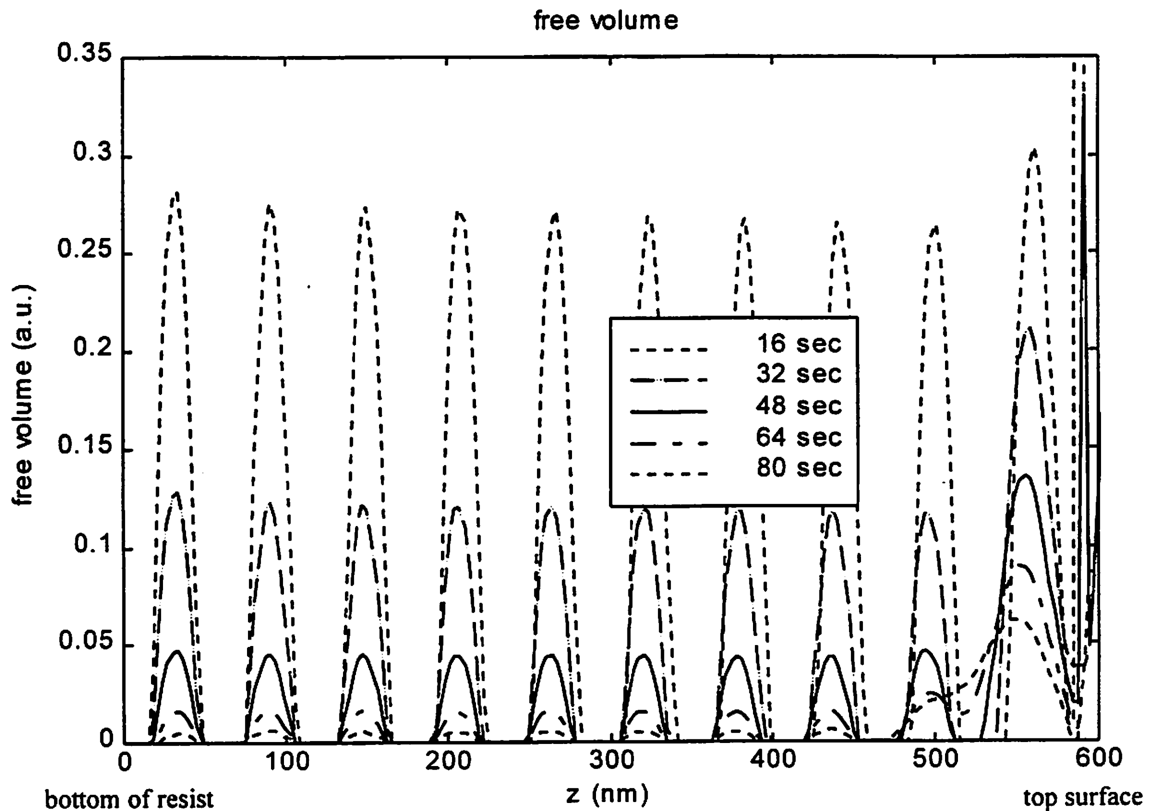

Figure 5.13 Free volume concentration at different time steps during PEB for UV5.

5.5.2 Parameter Extraction using Dynamic DITL Model

Using ASA as the optimization engine, we extract the eight parameters in the DITL model by fitting the experiment data with the simulation curve for both UV5 and AZ 2549, as shown in Figure 5.14 and Figure 5.15. The extraction result is listed in Table 5.5.

The fitting results seem better for UV5 than AZ 2549. There are many reasons that cause the deviation between experiment and simulation for AZ 2549. First, the setup did not allow for very accurate placement of the reflectometer spot within the 2mm exposed area. The reflected light from the exposed area makes the thickness measurement inaccurate. In contrast, for UV5 the thickness was measured off-line using an ellipsometer and the result is more accurate. Secondly, the experiment for AZ 2549 was done on the bake plate in the Berkeley MicroLab. The time was recorded manually, and after the wafer is placed on the bake plate, it took a few seconds for the temperature of the resist to ramp up to the desired PEB temperature. This caused the offset between the experiment and the simulation at the first few seconds. In contrast, for UV5 the experiment was done on a state-of-the-art wafer track, and both the time and the

temperature were controlled more accurately. If we can get *in situ* measurement of the temperature ramping during PEB for the AZ2549 resist, the program can be adapted to get a better fit.

Table 5.5 Results of Parameter Extraction using DITL Model

Parameter	UV5	AZ 2549
k_1	903.6	119.9
k_2 (sec^{-1})	3.45×10^{-2}	2.57×10^{3}
k_3 (sec^{-1})	9.54	2.28×10^{2}
k_4	9.55×10^{-4}	8.51×10^{-5}
D_{u0} (nm^2/sec)	0.0466	1.83×10^{-5}
a	7.61×10^{-6}	8.22×10^{-4}
D_w (nm^2/sec)	18.31	5.05
h_0	3.04×10^{-8}	8.51×10^{-3}
k_{loss} (sec^{-1})	6.32×10^{-2}	1.58×10^{-1}

Some of the parameters in Table 5.5 have counterparts in existing resist models. For example, k_2 corresponds to k_{amp}, its value given by the resist vendor is 0.0581 sec^{-1}, which is about 60% higher than what we extracted. The vendor value of k_{loss} is 0.0063 sec^{-1}, which is very close to what we obtained. The diffusion parameter values given by the vendor is very far away from those we extracted in Table 5.5, because in a flood exposure experiment, acid diffusion only occurs in the direction perpendicular to the wafer surface to smooth out the standing wave, and the thickness loss is not very sensitive to the diffusion coefficients.

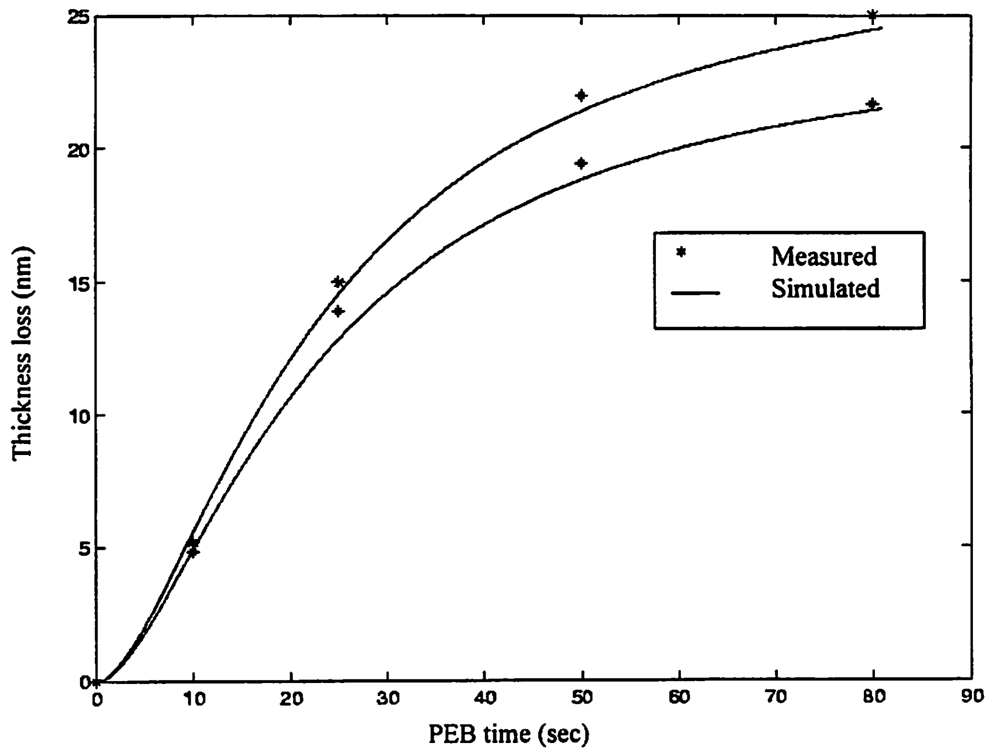

Figure 5.14 Thickness loss versus time during PEB for UV5.

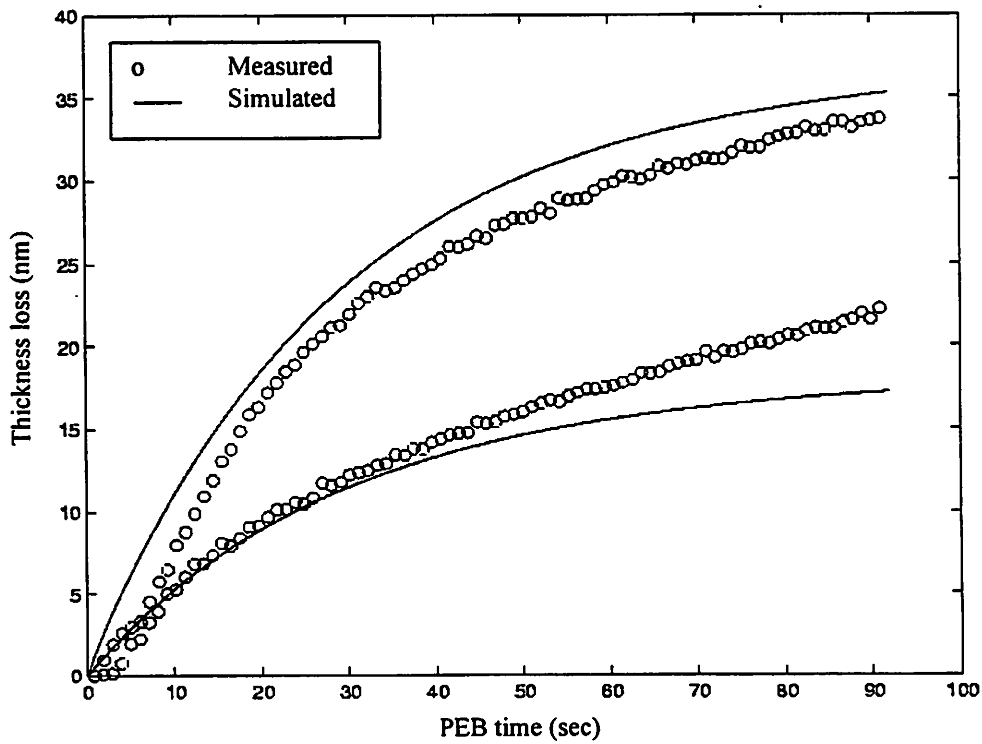

Figure 5.15 Thickness loss versus time during for AZ 2549.

5.6 Summary

In this chapter, we first set up a parameter extraction framework, and designed an experiment for the AZ2549 resist. Then experimental data were used to extract resist parameters using the static model. These parameter values are then fed into the dynamic model to extract more parameters.

Chapter 6 Conclusion

6.1 Summary

As stated in the *SIA International Technology Roadmap for Semiconductors*, optical lithography is still the mainstream approach for the industry, currently driven by developments in DUV technology for 100 nm CD applications. CD control is the limiting factor. Lithography simulation is playing a more and more important role in this evolution. Not only a good physically based model can provide useful insight to the lithography process in the research stage, but also a well calibrated lithography simulator can help optimize new recipes and do feedback and feed-forward control during product development and production.

In this work we have proposed both static and dynamic physical models for PEB in chemically amplified resists, and validated these models with experiments. The static model successfully models the quenching action in the resist across the complete exposure dose spectrum. The proposed dynamic model predicts well the volume shrinkage observed in resists for flood exposure, and could be used to gain insight in the resist mechanism. This insight may be of help in improving the current resist properties as well as in developing new resist systems.

After the models are validated, a framework is proposed to extract the parameters in the models using a minimum number of bake and develop experiments. While in this thesis only unpatterned experiments were used for parameter extraction, the same framework can be extended to patterned characterization experiments as well. [27] Adaptive simulated annealing is extensively used as the optimization engine for parameter extraction. Using the extracted parameter values, we can successfully fit the simulation curves to the experimental data.

6.2 Future Work

The numerical implementation of the DITL model in chapter 3 and the experiments we have done are for flood exposure only. In the summer of 1998, we have "seen" the thickness loss for patterned features after PEB using Atomic Force Microscope (AFM) at National

Semiconductor Corp. To model this effect in the presence of patterns in the resist, we can extend the program to a 2-dimensional case, and compare the simulated resist surface contour with the AFM measurement. The moving boundary method we proposed in chapter 3 can be easily adapted to 2-dimensional problems.

Since the dynamic DITL model has a physical basis, we can find close connections between the model parameters and the resist mechanism. For example, the parameter k_1 is used to convert the percentage deprotection to acid and volatile group concentration, and it shows the relation between the photoacid generator and the protecting t-BOC group. The parameter k_4 converts the number of voids to the amount of volume shrinkage, and its value gives an idea of the order of magnitude of the voids. Another example is the parameter k_{loss}, which illustrates how much the quenching effect is. With a careful design of experiment, these relations can be studied to help us further understand the resists.

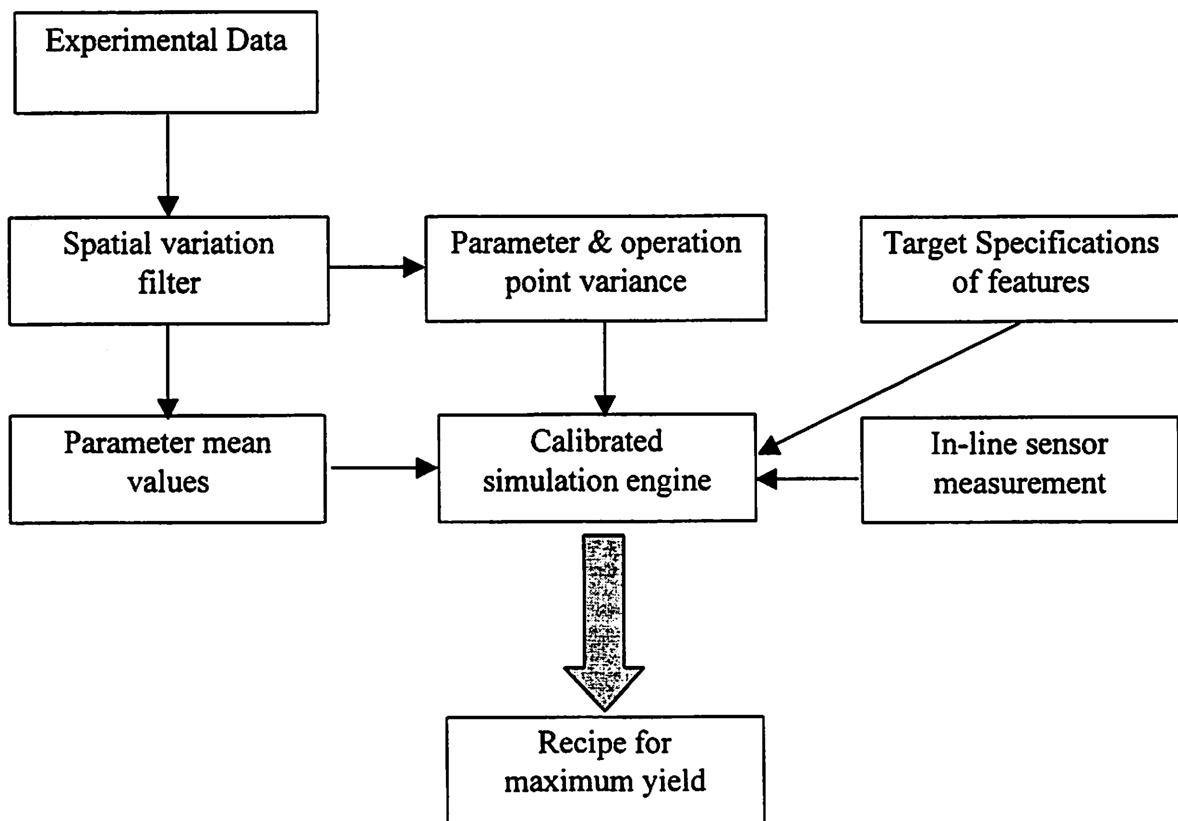

Figure 6.1 Parameter extraction and recipe optimization framework.

In order to efficiently utilize lithography simulators, it is necessary to know the sensitivity of the tuning parameters and their correlation under various experimental conditions. This may help decompose the high dimensional space into a few low dimensional subspaces, thus significantly accelerating the parameter extraction process.

With some additional efforts the process variation can also be extracted. This can be fed into the recipe optimization framework powered by a calibrated simulation engine (Figure 6.1) to enhance the yield. The maximum yield is obtained when the process output domain and the target specification domain have the maximum overlap, as shown in Figure 6.2.

As more and more *in situ* sensors are being integrated on the wafer track, more and more quantities about the wafer status can be obtained while the wafer is being processed. With a well calibrated simulation engine, an advanced run-to-run controller can feed this information forward to correct process settings for later steps, and feed the information back for the processing conditions for the next wafer. We believe that run-to-run control would help significantly reduce the CD variation in current and future generation lithography technologies.

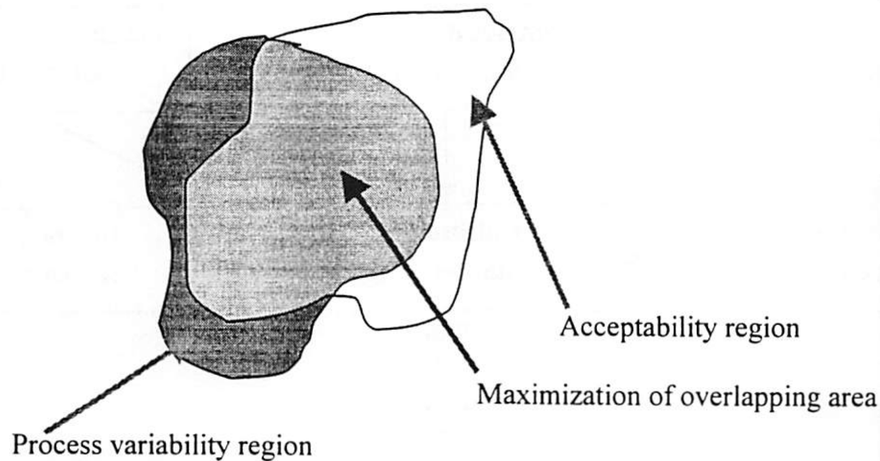

Figure 6.2 The goal of recipe optimization

References

[1] Semiconductor Industry Association, "The International Technology Roadmap for Semiconductors: Lithography", *1999*

[2] Berkeley TCAD Software Tools, http://tanqueray.eecs.berkeley.edu/tcad/tcad.html

[3] FINLE Technologies, P.O. Box 162712, Austin, TX 78716

[4] Sigma-C GmbH, 901 Campisi Way, #248, Campbell, CA 95008

[5] Semiconductor Industry Association, "The International Technology Roadmap for Semiconductors: Modeling and Simulation", *1999*

[6] M. Zuniga, G. Wallraff, E. Tomacruz, B. Smith, C. Larson, W.D. Hinsburg, A.R. Neureuther, "Simulation of locally enhanced three-dimensional diffusion in chemically amplified resists", *Journal of Vacuum Science & Technology B, Nov.~Dec. 1993, vol. 11, pp. 2862-66*

[7] M.A. Zuniga, A.R. Neureuther, "Reaction-Diffusion Modeling and Simulations in Positive DUV Resists", *Journal of Vacuum Science & Technology B, Nov.~Dec. 1995, vol. 13, pp. 2957-62*

[8] M.A. Zuniga, A.R. Neureuther, "Stress dependent silylation model and two-dimensional profile simulation", *Journal of Vacuum Science & Technology B, Nov.~Dec. 1997, vol.15, No. 6, pp.2565-9*

[9] E. Croffie, M. Cheng, A. Neureuther, "Moving boundary transport model for acid diffusion in chemically amplified resists", *Journal of Vacuum Science & Technology B, Nov.~Dec. 1999, vol. 17, pp. 3339-44*

[10] E. Croffie, M. Cheng, A. Neureuther, F. Houlihan, R. Cirelli, J. Sweeney, G. Dabbagh, P. Watson, O. Nalamasu, I. Rushkin, O. Dimov, A. Gabor, "Modeling chemically-amplified resists for 193nm lithography", *SPIE vol. 3999, 2000*

[11] E. Croffie, "Moving boundary models and methods for deep submicron resist process simulation", *M.S. Thesis, Memorandum No. UCB/ERL M99/26, May 20, 1999*

[12] N. Jakatdar, J. Bao, C. Spanos, R. Subramanian, B. Rangarajan, "Physical modeling of deprotection induced thickness loss", *SPIE vol. 3678, 1999*

[13] S.V. Postnikov, M.D. Stewart, H.V. Tran, M.A. Nierode, D.R. Medeiros, T. Cao, J. Byers, S.E. Webber, C.G. Wilson, "Study of resolution limits due to intrinsic bias in chemically amplified photoresists", *Journal of Vacuum Science & Technology B, Nov.~Dec. 1999, vol. 17, pp. 3335-8*

[14] C.R. Szmanda, R.L. Brainard, J.F. Mackevich, A. Awaji, T. Tanaka, Y. Yamada, J. Bohland, S. Tedesco, B. Dal'Zotto, W. Bruenger, M. Torkler, W. Fallmann, H. Leoschner, R. Kaesmaier, P.M. Nealey, A.R. Pawloski, "Measuring acid generation efficiency in chemically amplified resists with all three beams", *Journal of Vacuum Science & Technology B, Nov.~Dec. 1999, vol. 17, pp. 3356-61*

[15] H. Ito, C.G. Wilson, "Application of photoinitiators to the design of resists for semiconductor manufacturing", *Polymers in Electronics, ACS Symposium Series 242 (1984) pp. 11-23*

[16] Y. Yoshimura, Y. Nakayama, S. Okazaki, "Acid diffusion effect on nanofabrication in chemical amplification resist", ", *Journal of Vacuum Science & Technology B, Nov.~Dec. 1992, vol..10, pp. 2615-9*

[17] C.A. Mack, "Inside PROLITH – A Comprehensive Guide to Optical Lithography Simulation", *Feb. 1997*

[18] J. Byers, et al. "Characterization and Modeling of a Positive Amplified Resist", *SPIE vol. 2438, pp. 153-166, 1995*

[19] C.A. Mack, "Development of Positive Photoresist", *Journal of Electrochemical Society, Vol. 134, No.1, Jan 1987, pp. 148-152*

[20] Pain, L.; Le Cornec, C.; Rosilio, C.; Paniez, P.J. "Free volume variations during exposure and PEB of DUV positive resists: Effect on dissolution properties", *Proceedings of the SPIE - The International Society for Optical Engineering, vol.2724, (Advances in Resist Technology and Processing XIII, Santa Clara, CA, USA, 11-13 March 1996.) SPIE-Int. Soc. Opt. Eng, 1996. p.100-9*

[21] W.H. Press, S.A. Teukolsky, W.T. Vetterling, B.P. Flannery, "Numerical Recipes in C – The Art of Scientific Computing", *Cambridge University Press, 1992*

[22] N. Metropolis, A.W. Rosenbluth, A.H. Teller, E. Teller, "Equation of State Calculations by Fast Computing Machines", *Journal of Chem. Phys. 21 (6), pp1087-92 (1953)*

[23] S. Kirkpatrick, C.D. Gelatt Jr., M.P. Vecchi, "Optimization by Simulated Annealing", *Science **220** (4598), 671-80 (1983)*

[24] C. Sechen, D. Braun, A. Sangiovanni-Vincentelli, "ThunderBird: A Complete Standard Cell Layout Package", *IEEE Journal of Solid-State Circuits, vol. 23, No. 2, 410-20, April 1988*

[25] S. Devadas, A.R. Newton, "Algorithm for Hardware Allocation in Data Path Synthesis", *IEEE Trans. on Computer-Aided Design of Integrated Circuits and Systems, vol. 8, No. 7, 768-81, July 1989*

[26] L. Ingber, "Simulated Annealing: Practice versus Theory", *Mathematical and Computer Modeling, vol. 18, No. 11, 29-57, 1993*

[27] H. Szu, R. Hartley, "Fast Simulated Annealing", *Phys. Lett. A 122 (3-4), 157-62, 1987*

[28] L. Ingber, "Adaptive Simulated Annealing (ASA): Lessons Learned", *Control and Cybernetics on "Simulated Annealing Applied to Combinatorial Optimization", 1995*

[29] L. Ingber, "Generic Mesoscopic Neural Networks based on Statistical Mechanics of Neocortical Interactions", *Phys. Rev. A 45 (4), R2183-86, 1992*

[30] S. Geman, D. Geman, "Stochastic Relaxation, Gibbs Distribution and the Bayesian Restoration in Images", *IEEE Trans. Patt. Anal. Mac. Int. 6 (6), 721-41, 1984*

[31] D.E. Aspnes, J.B. Theeten, F. Hottier, "Investigation of Effective-Medium Models of Microscopic Surface Roughness by Spectroscopic Ellipsometry", *Phys. Rev. B, vol. 20, No. 8, 3293-3302, Oct. 1979*

[32] A.R. Forouhi, I. Bloomer, "Optical Properties of Crystalline Semiconductors and Dielectrics", *Phys. Rev. B, vol. 38, No. 3, 1865-74, July, 1988*

[33] G.E. Jellison Jr., F.A. Modine, "Parameterization of the Optical Functions of Amorphous Materials in the Interband region", *App. Phys. Lett., 15, vol. 69, No. 3, 371-73, July, 1996*

[34] W.A. McGahan, T. Makovicka, J. Hale, J.A. Woollam, "Modified Forouhi and Bloomer Dispersion Model for the Optical Constants of Amorphous Hydrogenated Carbon Thin Films", *Thin Solid Films, vol. 253, 1994*

[35] X. Niu, "An Integrated System of Optical Metrology for Deep Sub-Micron Lithography", *Ph.D. thesis, Memorandum No. UCB/ERL M99/27, April 1999*

[36] N. Jakatdar, "Deep sub-micron photolithography control through in-line metrology", *Ph.D. thesis, Memorandum No. UCB/ERL M00/11, January, 2000*

[37] J. Crank, "Free and Moving Boundary Problems", *Clarendon Press, Oxford, 1984*

Appendix A List of Figures

Figure 2.1	PAG decomposition during exposure	4
Figure 2.2	Deprotection during PEB	4
Figure 2.3	Deprotection vs. dose at different PEB temperature	6
Figure 2.4	Deprotection and diffusion during PEB	10
Figure 3.1	Convergence test results for various time steps	18
Figure 3.2	Space step size adjustment after each time step	19
Figure 3.3	Two-dimensional fixed grid size method	20
Figure 3.4	Grid-size tracking method for 2D moving-boundary problem	21
Figure 4.1	Incidence of plane electromagnetic wave upon two media interface	28
Figure 4.2	Reflection of plane electromagnetic wave from a single layer of thin film	29
Figure 4.3	Pseudo-code for multilayer thin film reflection	30
Figure 4.4	Resist index and thickness extraction framework	31
Figure 5.1	General parameter extraction framework	34
Figure 5.2	In-situ reflectivity spectrum during PEB	36
Figure 5.3	Comparison of measured and fitted reflectivity at 17th second	37
Figure 5.4	Resist thickness change during PEB	37
Figure 5.5	Fitting experiment data with reduced effective dose model	38
Figure 5.6	Fitting UV5 experiment data with quencher reaction model at 135°C	39
Figure 5.7	Static model fitting experimental data for UV5 at different PEB temperature	40
Figure 5.8	Static model fitting experimental data for AZ2549 at PEB temperature 110°C	41
Figure 5.9	Develop rata versus the normalized concentration of unreacted sites for UV5	43
Figure 5.10	Acid concentration at different time steps during PEB for UV5	43
Figure 5.11	Percentage deprotection at different time steps during PEB for UV5	45
Figure 5.12	Volatile group concentration at different time steps during PEB for UV5	45
Figure 5.13	Free volume concentration at different time steps during PEB for UV5	46
Figure 5.14	Thickness loss versus time during PEB for UV5	48
Figure 5.15	Thickness loss versus time during PEB for AZ 2549	48

Figure 6.1 Parameter extraction and recipe optimization framework 52
Figure 6.2 The goal of recipe optimization 53

Appendix B List of Symbols

Parameter	Description	Unit
α	Absorption coefficient of the resist film	nm^{-1}
Δt	Time step for finite difference method	sec
Δz	Space step for finite difference method	nm
γ	Electromagnetic wave transmission at media interface	--
$\tilde{\eta}$	Complex refraction index	--
λ	Light wavelength	nm
ϖ	Volume element	nm^3 or nm
ξ	Concentration variable (such as u, v, w, h) distribution function	--
a	Acid diffusivity amplification factor	--
[Acid]	Acid concentration	nm^{-3}
A_c	Cauchy coefficient	--
A_i	Lower bound for parameter p_i	--
B_c	Cauchy coefficient	nm^2
B_i	Upper bound for parameter p_i	--
c_{cost}	Cooling scaling factor for the acceptance function for ASA	--
c_i	Cooling scaling factor for T^i	--
C	Photoacid formation coefficient	cm^2/mJ
C_c	Cauchy coefficient	nm^4
C_p	Parameter constraint	--
d	Film (resist) thickness	nm
D	Parameter dimensionality for simulated annealing	--
D_c	Cauchy coefficient	nm
$Dose_{eff}$	Effective dose, corrected by quenching effect	mJ/cm^2
Dose	Exposure dose	mJ/cm^2
$Dose_q$	Effective quenching dose	mJ/cm^2
D_s	Exposure dose, corrected by the reflectivity at the air-resist interface	mJ/cm^2

Parameter	Description	Unit
D_u	Acid diffusivity	nm^2/sec
D_w	Volatile group diffusivity	nm^2/sec
E_{accept}	Energy of the last accepted state	--
E_c	Cauchy coefficient	nm^3
E_k	Energy of the kth state	--
F_c	Cauchy coefficient	nm^5
$g(\bar{p}, T_k)$	Probability density of D-dimensional variable $\bar{p}$	--
g_k	Probability that a point $\bar{p} \in C_p$ is sampled at step k	--
h	Normalized void (hole) concentration	--
$h(\Delta E, T_k)$	Probability for acceptance of new state	--
k	Imaginary part of the refractive index	--
k_1	Scaling factor to convert deprotection into corresponding Volatile group concentration	--
k_2	Deprotection reaction rate coefficient	sec^{-1}
k_3	Void relaxation rate	sec^{-1}
k_4	Scaling factor to convert voids collapsed into volume shrinkage	--
k_α	Neutralization reaction coefficient	sec^{-1}
k_{amp}	Acid amplification factor	sec^{-1}
k_{cost}	Number of acceptance for ASA	--
k_{loss}	Acid loss factor	sec^{-1}
m	Normalized concentration of unreacted blocking site in resist	--
m_{th}	Threshold PAC concentration	--
n	Real part of the refractive index	--
n_s	dissolution selectivity parameter	--
$\bar{p}$	Parameter vector for the function to be optimized	--
$p_{1,2,...}$	Component of parameter vector $\bar{p}$	--
$\bar{p}_{accept}$	Last accepted input parameter vector	--
$\bar{p}_k$	Input parameter vector at k^{th} step	--
$[PAG]_0$	Initial PAG concentration	nm^{-3}
Q	Normalized quencher concentration	--
r	Reflectivity coefficient	--

Parameter	Description	Unit
R	Universal gas constant (Chapter 2)	$cal \cdot mol^{-1} \cdot K^{-1}$
R	Intensity reflectivity (Chapter 4)	--
R^m	m dimensional linear space	--
R_{max}	Maximum development rate	nm/sec
R_{min}	Minimum development rate	nm/sec
s_k^i	Number of generations for p_i up to step k	--
t	Time	sec
T	Absolute temperature	K
T_0	Initial "temperature" for simulated annealing	--
$T_{0,cost}$	Initial cost "temperature"	--
T_k	Annealing "temperature" at step k for simulated annealing	--
$T_{k,cost}$	Cost "temperature" at step k	--
T_0^i	Initial "temperature" for parameter p_i for ASA	--
T_k^i	Annealing "temperature" for parameter p_i at step k for ASA	--
u	Normalized acid concentration	--
u_i	Uniformly distributed random number at [0, 1]	--
v	Percentage deprotection	--
w	Normalized volatile group concentration	--
x	Direction parallel to resist surface	--
$\bar{x}$	Input vector for the function to be optimized	--
$x_{1,2,...}$	Components of input vector $\bar{x}$	--
z	Depth into the resist	nm